Synchrotron X-Ray Diffraction Topography of Semiconductor Heterostructures

Aapo Lankinen

Synchrotron X-Ray Diffraction Topography of Semiconductor Heterostructures

Aapo Lankinen

A doctoral dissertation completed for the degree of Doctor of Science (Technology) to be defended, with the permission of the Aalto University School of Electrical Engineering, at a public examination held at the lecture hall TU1 of the school on 14th of December 2012 at 12 noon.

Aalto University
School of Electrical Engineering
Department of Micro- and Nanosciences
Nanotechnology Group

441   697
Printed matter

Author

Aapo Lankinen

Name of the doctoral dissertation

Synchrotron X-Ray Diffraction Topography of Semiconductor Heterostructures

Publisher School of Electrical Engineering

Unit Department of Micro- and Nanosciences

Series Aalto University publication series DOCTORAL DISSERTATIONS 173/2012

Field of research Nanotechnology

Manuscript submitted 20 June 2012 | **Date of the defence** 14 December 2012

Permission to publish granted (date) 4 October 2012 | **Language** English

☐ **Monograph** | ☒ **Article dissertation (summary + original articles)**

Abstract

In this thesis dislocations, other crystal defects, and strain in compound heterostructures were studied by means of synchrotron radiation X-ray topography and other X-ray methods. Also, models for critical thickness of thin films were compared to experimental results. Synchrotron radiation X-ray topography (SR-XRT) is an ideal method for studying strained heterostructures with relatively few dislocations ($< 10^4 \, cm^2$).

Crystal defects in GaAs ans InAs p-i-n structures were characterized. Misfit dislocations and critical thickness in epitaxial dilute GaAsN on GaAs was characterized with synchrotron radiation X-ray topography and high-resolution X-ray diffractometry. Defect structure of thin GaAs epitaxial layer on Ge substrates was studied. Strain distribution between GaN thin films and sapphire substrate was analyzed from back-reflection synchrotron X-ray topographs, and cellular network of strain with about 30 micrometer cell size was discovered. Epitaxial quality of the GaN layers was analyzed. InP epitaxial lateral overgrowth layers were analyzed with synchrotron radiation X-ray topography and high-resolution X-ray diffraction, and strain fields around the growth window edges were successfully imaged.

Reciprocal space maps (RSM) were measured from GaInP on GaAs buffer on Ge substrate heterostructures, and no relaxation was observed in neither sample, which proves that a very small number of misfit dislocations is only detectable with SR-XRT. Critical thickness models were compared with experimental data for the GaInP thin film on GaAs buffer on Ge substrate heterostructure, and new insight was found about the relation of pyramidical hillock defects to misfit dislocation formation. Also, the crystal structure of the pyramidical hillocks was determined, and it was found that they are composed of InP instead of GaInP as previously thought. The critical thickness model was successfully expanded to take thermal expansion into account.

The information about crystal defects and their distribution, and analysis methods to study them, which was acquired in this thesis, can be used to better understand and control crystal defects in semiconductor heterostructures.

Tiivistelmä

Tässä työssä tutkittiin dislokaatioiden, muiden kidevirheiden ja hilajännityksen esiintymistä heterorakenteisissa yhdistepuolijohteissa käyttämällä synkrotroniröntgentopografiaa ja muita röntgenmittausmenetelmiä. Työssä vertailtiin myös erilaisten epitaktisten hilarakenteiden kriittisen paksuuden mallien antamia tuloksia kokeellisiin tuloksiin. Synkrotroniröntgen-topografia (SR-XRT) osoittautui verrattomaksi mittausmenetelmäksi sellaisten yhdiste-puolijohteiden tutkimiseen, joissa on vähän dislokaatioita ($< 10^4$ cm^2) ja jotka ovat sisäisessä jännitystilassa.

GaAs- ja InAs-pohjaisista p-i-n -rakenteista tutkittiin kidevirheitä. Alustakiekon (GaAs) päälle kasvatetuista laimeista GaAsN-kalvoista tutkittiin sovitusdislokaatioiden syntyä ja kriittistä paksuutta käyttämällä synkrotroniröntgentopografiaa ja röntgendiffraktometriaa. Samoin tutkittiin kidevirheitä Ge-alustan päälle kasvatetusta ohuesta GaAs-kalvosta. Hilajännityksen jakautuminen safiirialustan päälle kasvatetun GaN-kalvon rajapinnassa selvitettiin koostuvan noin 30 mikrometrin silmäkoon virheverkosta. Kasvatetun GaN-kalvon laatu analysoitiin synkrotroniröntgentopografialla. Piialustalle sivusuuntaan maskin päälle kasvatettujen epitaktisten InP-kalvojen sisäiset ja kasvatusaukkoon jättämät jännitystilat tutkittiin synkrotroniröntgentopografialla ja röntgendiffraktometrialla.

Ge-substraatin ja GaAs-puskurikerroksen päälle kasvatetuista GaInP-kalvoista mitattiin käänteishilakarttoja, joista todettiin että kalvojen jännitys ei ollut havaittavasti purkautunut, mikä puolestaan todistaa että hyvin pieni määrä sovitusdislokaatioita saadaan näkyviin vain röntgentopografialla. Kriittisen paksuuden malleja vertailtiin kokeellisiin tuloksiin GaInP-kalvoilla, ja saatiin uutta tietoja GaInP-kalvoissa esiintyvien mikropyramidien ja sovitusdislokaatioiden yhteydestä. Mikropyramidien koostumus (InP) ja kiderakenne selvitettiin, ja tieto oli vastoin aikaisempaa oletusta (GaInP) mikropyramidien koostumuksesta. Kriittisen paksuuden mallia laajennettiin onnistuneesti ottamalla lämpölaajeneminen huomioon.

Työssä löydettiin uutta tietoa kidevirheistä ja niiden esiintyvyydestä, sekä niiden tutkimiseen käytettävistä menetelmistä. Näiden tietojen avulla heteropuolijohderakenteiden kidevirheitä voidaan ymmärtää ja hallita paremmin.

Preface

"Jokainen tsäänssi on mahdollisuus!" – Matti Nykänen
(Every chance is an opportunity)

Helsinki, November 2012   Aapo Lankinen

Contents

List of Publications

This thesis consists of an overview and of the following publications, which are referred to in the text by their Roman numerals.

I   A. Lankinen, T. Tuomi, J. Riikonen, L. Knuuttila, H. Lipsanen, M. Sopanen, A. Danilewsky, P.J. McNally, L. O'Reilly, Y. Zhilyaev, L. Fedorov, H. Sipilä, S. Vaijärvi, R. Simon, D. Lumb and A. Owens, *Synchrotron X-ray topographic study of dislocations and stacking faults in InAs*, Journal of Crystal Growth **283** (2005) 320–327.

II   L. Knuuttila, A. Lankinen, J. Likonen, H. Lipsanen, X. Lu, P. McNally, J. Riikonen and T. Tuomi, *Low Temperature Growth GaAs on Ge*, Japanese Journal of Applied Physics **44** (2005) 7777–7784.

III A. Lankinen, T. Tuomi, M. Karilahti, Z.R. Zytkiewicz, J.Z. Domagala, P.J. McNally, Y-T. Sun, F. Olsson and S. Lourdudoss, *Crystal Defects and Strain of Epitaxial InP Layers Laterally Overgrown on Si*, Crystal Growth & Design **6** (2006) 1096–1100.

IV   A. Lankinen, L. Knuuttila, T. Tuomi, P. Kostamo, A. Säynätjoki, J. Riikonen, H. Lipsanen, P. J. McNally, X. Lu, H. Sipilä, S. Vaijärvi and D. Lumb, *Synchrotron X-ray topography study of defects in epitaxial GaAs on high-quality Ge*, Nuclear Instruments and Methods in Physics Research A **563** (2006) 62–65.

V   O. Reentilä, A. Lankinen, M. Mattila, A. Säynätjoki, T.O. Tuomi, H. Lipsanen, L. O'Reilly and P.J. McNally, *In-situ optical reflectance and synchrotron X-ray topography study of defects in epitaxial dilute GaAsN on GaAs*, Journal of Materials Science: Materials in Electronics **19** (2008) 137–142.

VI   A. Lankinen, T. Lang, S. Suihkonen, O. Svensk, A. Säynätjoki, T.O. Tuomi, P.J. McNally, M. Odnoblyudov, V. Bougrov, A.N. Danilewsky, P. Bergman and R. Simon, *Dislocations at the interface between sapphire and GaN*, Journal of Materials Science: Materials in Electronics **19** (2008) 143–148.

VII A. Säynätjoki, T.O. Tuomi, A. Lankinen, P.J. McNally, A. Danilewsky, Y. Zhilyaev and L. Fedorov, *Dislocations of GaAs p-i-n diodes grown by*

hydride vapour phase epitaxy, Journal of Materials Science: Materials in Electronics **19** (2008) 149–154.

VIII   P. Kostamo, A. Lankinen, A. Säynätjoki, H. Lipsanen, T.O. Tuomi, Y. Zhilyaev, L. Fedorov and T. Orlova, *Synchrotron X-Ray topography and electrical characterization of epitaxial GaAs p-i-n structures*, Nuclear Instruments and Methods in Physics Research A **591** (2008) 192–195.

IX   A. Lankinen, L. Knuuttila, P. Kostamo, T.O. Tuomi, H. Lipsanen, P.J. McNally and L. O'Reilly, *Synchrotron topography and X-ray diffraction study of GaInP layers grown on GaAs/Ge*, Journal of Crystal Growth **311** (2009) 4619–4627.

Author's contribution

The author of this thesis wrote the manuscripts for Publications I, III, IV, VI, and IX, and parts of the manuscripts for Publications V and VIII. The author designed the measurements in Publications I, III, IV, VI, and IX, and designed the measurements with co-authors for Publication V and VII.

The author recorded the synchrotron topographs for Publications I, V, VI, and IX, recorded about half of the topographs for Publication IV, and participated in recording the topographs with the co-authors in Publications II, VII, and VIII. The author analyzed the topographs and Laue patterns for Publication I, III, IV, V, VI, and IX, and participated in the analysis with the co-authors for Publications II, VII, and VIII.

The author performed the XRD, HR-XRD and reciprocal space maps measurements for Publications III and IX, and made half of the HR-XRD measurements for Publication V. The author analyzed the XRD, HR-XRD and reciprocal space map data for Publications III and IX, and made the analysis together with the a co-author for Publication V. The author made the $\vec{g} \cdot \vec{b} = 0$ dislocation type analysis for Publications I, V, and IX, and made the critical thickness analysis for Publications V and IX. The author analyzed the structure of the crystalline InP pyramids in Publication IX.

List of Abbreviations

Abbreviation	Meaning
ANKA	Angstromquelle Karlsruhe, a synchrotron facility
CCD	Charge-coupled device, detector in cameras
DESY	Deutsches Elektronen-Synchrotron, a synchrotron facility
DORIS III	Double Ring Store III, a synchrotron storage ring in DESY
ELO	Epitaxial lateral overgrowth
FWHM	Full width half maximum
HASYLAB	Hamburger Synchrotronstrahlungslabor
HR-XRD	High resolution X-ray diffraction
HVPE	Hydride vapor phase epitaxy
LPE	Liquid phase epitaxy
MBE	Molecular beam epitaxy
MD	Misfit dislocation
MOVPE	Metal-organic vapor phase epitaxy
RSM	Reciprocal space map
RT	Room temperature
SPE	Solid phase epitaxy
SR-XRT	Synchrotron radiation X-ray topography
VPE	Vapor phase epitaxy
XRD	X-ray diffraction

List of Symbols

Symbol	Meaning
a	Lattice constant of a cubic crystal
a_f, a_s	Thin film and substrate lattice constants
$\vec{a}_1$, $\vec{a}_2$, $\vec{a}_3$	Lattice base vectors in three dimensions
$\vec{b}$	Burgers vector, i.e. a measure of lattice displacement
c	Speed of light in vacuum
d	Lattice spacing of atom planes in a crystal
E	Electron or positron total energy in a synchrotron
$f = \Delta a/a$	Relative lattice mismatch of a thin film to a substrate
f_n	Atomic scattering factor
$\mathcal{F}_{hkl}$	Structure factor of diffraction hkl from a unit cell
$\mathcal{F}_0''$	Zeroth order of the imaginary part of the structure factor
$\mathcal{F}_g''$	Fourier coefficient of order $|\vec{g}|$ of the imaginary part
	of the structure factor
$\vec{g}$	Diffraction vector
h	Thin film thickness
h_c	Thin film critical thickness, calculated or measured
h, k, l	Miller indices of a crystal plane, always integers
$\hbar$	Planck's constant h divided by 2π
$\mathcal{I}$	Synchrotron X-ray radiation energy per positron or electron
I_c	Electron or positron current of a synchrotron
$\vec{k}'$, $\vec{k}$	Incident and diffracted X-ray beams, respectively
$K_{1/3}(\xi)$	Modified Bessel function of the 2$^{\text{nd}}$ kind, fractional order $1/3$
$K_{2/3}(\xi)$	Modified Bessel function of the 2$^{\text{nd}}$ kind, fractional order $2/3$
$\vec{\ell}$	Dislocation line direction
L	Source-to-sample distance in synchrotron topography
m_0	Electron or positron rest mass
mrad	milliradian, 10^{-3} radians
N_u	Number of atoms in the unit cell of a crystal
$\mathcal{N}$	Atomic number density of a crystal, $\mathcal{N} = N_u/V_u$
n	Order of the diffraction
$\vec{n}$	Sample surface normal
q	Elemental charge
$\vec{q}_1$, $\vec{q}_2$, $\vec{q}_3$	General reciprocal lattice base vectors
$\vec{q}_x$, $\vec{q}_y$, $\vec{q}_z$	Reciprocal lattice base vectors of the cubic lattice
r_F, r_0	Spatial resolution of X-ray sensitive film or other detector
r_x, r_z	Horizontal and vertical resolutions of a synchrotron experiment

S	Lattice plane of a crystal
$\vec{s}$	Normal vector of the lattice plane
t	Sample thickness
$\vec{u}$	Misfit dislocation line direction
u, v, w	Coordinates in real space for lattice base vectors $\vec{a}_1, \vec{a}_2, \vec{a}_3$
V_u	Volume of the unit cell of a crystal, $V_u = \vec{a}_1 \cdot (\vec{a}_2 \times \vec{a}_3)$
x	Sample-to-detector distance in synchrotron topography
z	Penetration depth of X-rays
Z	Atomic number of an element
Å	Ångström, 10^{-10} m
α_b	Angle between Burgers vector $\vec{b}$ and dislocation line $\vec{u}$
α_c	Critical incident angle for total X-ray reflection
α_{ltc}	Linear thermal expansion coefficient of a material
γ	Relativistic Lorentz factor, $\gamma = (1 - v^2/c^2)^{-1/2}$
Γ	Parameterized term in the critical thickness equation
ϵ_0	Permittivity of vacuum
ε_0	Ratio of the the imaginary structure factor parts $\mathcal{F}''_g$ and $\mathcal{F}''_0$
$\varepsilon_x, \varepsilon_y$	Horizontal and vertical emittances of a synchrotron
ζ	Attenuation length of X-rays
θ, θ_{hkl}	Bragg angle
2θ	Diffraction angle, i.e. twice the Bragg angle
ϑ	Angle between the synchrotron plane and the X-rays
λ, λ_{hkl}	X-ray wavelength
λ_b	Angle between Burgers vector $\vec{b}$ and vector $\vec{u} \times \vec{n}$
μ_0	Average linear X-ray attenuation coefficient of a sample at X-ray wavelength λ
ν	Poisson ratio
ξ	Parameter in the synchrotron radiation flux equation
ρ	Instantaneous synchrotron orbit radius
σ_x, σ_z	Standard deviations of the spatial distribution of synchrotron radiation particle orbits
Σ_x, Σ_z	FWHM spatial sizes of the synchrotron particle orbits
ϕ	Angle of rotation about surface normal, i.e. azimuthal angle
Φ	Synchrotron X-ray photon flux
ψ	Tilt angle in a plane perpendicular to the diffraction plane and sample surface
ω	Angle between the incident X-ray beam and sample surface
ω_s	The angular frequency of the X-rays of a synchrotron
Ω_s	The solid angle of the radiation cone of a synchrotron
Ω	Parameterized term in the critical thickness equation

1 Introduction

In this thesis defects in crystal heterostructures consisting of group IV elemental semiconductors and III/V compound semiconductors were studied by means of synchrotron radiation X-ray topography (SR-XRT) and X-ray diffraction (XRD). The sample crystals include epitaxial structures with highly doped layers, dilute-layer heterostructures, two-layer heterostructures, and multilayer heterostructures. Crystals are pieces of solid material, whose constituent atoms or molecules are arranged in a periodic pattern in all the three spatial dimensions. The modern word "crystal" is derived from the Greek word $\kappa\rho\upsilon\sigma\tau\alpha\lambda\lambda o\xi$ (*krustallos*, ice) [1]. The rigid arrangement of the constituents is the key property of crystals, which possess both orientational and translational symmetry of *crystal lattice* positions over their whole volume. There are 7 possible crystal systems, which are sub-classed into 14 distinct *Bravais lattices* that contain the 230 crystallographic space groups of the three-dimensional space [2]. All true crystals are members of exactly one of these crystal systems and groups, but in practice the Bravais lattice type is often sufficient for categorizing different crystals. The Bravais lattices are built by repeating small parallelepipeds through space. The parallelepipeds are called *the unit cells*, which typically contain only a few atoms in the case of the inorganic crystals. An additional class of materials called *quasicrystals* has been discovered [3], but because the quasicrystals do not possess true long-range periodicity or exact rotational symmetry, they do not fulfill the classical definition of a crystal, despite their crystal-like properties caused by localized symmetries and long-range order.

The semiconductor samples studied in this work are all true crystals, and they belong to the *cubic* and *hexagonal* crystal systems. The epitaxial compound semiconductors analyzed in Publications I–V and VII–IX are GaAs, GaAsN, InAs, InP, and GaInP, which all crystallize into *the zincblende lattice*. Figure 1.1 a) is an illustration of the zincblende unit cell having two elements labeled A and B. The substrate crystals of the samples of Publications II–IV and IX are Si and Ge, which crystallize into *the diamond lattice*. The diamond lattice has the same atom positions as the zincblende lattice, but instead of two distinct elements it has only one atom species. One of the articles, Publication VI, discusses crystal quality of GaN films grown on sapphire, on which GaN always crystallizes in the hexagonal wurtzite lattice. Beside the wurtzite lattice, GaN crystals may grow in the cubic phase, but the wurtzite form is more common. The hexagonal wurtzite lattice is illustrated in Fig. 1.1 b).
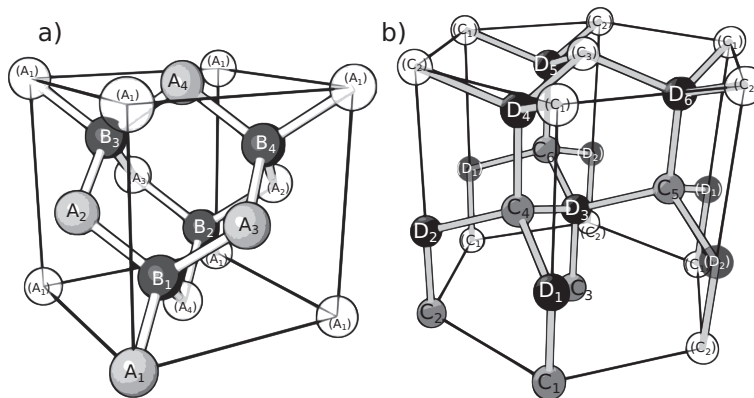
Figure 1.1: **a)** Zincblende unit cell consists of 8 atoms of 2 elements, here labeled A_1–A_4 and B_1–B_4. **b)** Hexagonal wurtzite cell consists of 12 atoms of 2 elements, here labeled C_1–C_6 and D_1–D_6. In both **a)** and **b)** the nearest neighbors are connected with thick lines. Also, the atoms belonging to the neighboring cells are drawn translucent and indicated with bracketed labels.

Monocrystals, i.e. single crystals, are solid pieces of matter having their whole volume repeating the same pattern of atoms. The size of crystals vary considerably, and the biggest monocrystals may measure several meters. All samples studied in Publications I–IX were monocrystals, except the InP epitaxial lateral overgrowth (ELO) structures of Publication III, which had small-angle crystal boundaries, and they could thus be labeled either mono- or polycrystals depending on a matter of opinion. Polycrystals consist of small crystallites that are interconnected through crystal boundaries. The crystallite boundaries contain a large number of dislocations, which are the result of connecting two lattices with adverse orientation on the boundary. The size and orientation of the crystallites in the polycrystalline matter may vary considerably depending on the composition and growth conditions of the crystallites. A sample having crystallites oriented almost similarly, so that the angles between the crystallite lattices are very small, may in extreme cases be somewhere half-way between mono- and polycrystalline. Such a sample could be a polycrystal with unusually small boundary angles, or simply a monocrystal with numerous dislocations in a specific pattern. Notwithstanding the ambiguous transition from monocrystals to polycrystals, the size of the crystallites in a polycrystalline matter can be anything between few tens of nanometers to few millimeters, after which the crystallites would typically be called small monocrystals.

2 Experimental Techniques

2.1 X-Ray Diffractometry

After the initial discovery of X-rays by W.C. Röntgen in 1895, the X-rays were immediately used for recording absorption images on photographic plates [4]. A few years later, X-Ray diffraction by crystals was first discovered by W. Friedrich, P. Knipping, and M. von Laue [5, 6, 7]. The discovery of a physical law connecting the X-ray wavelength and the reflection angle in the X-ray diffraction by W. L. Bragg [8] opened up the possibility to study the exact coordination of the atoms in crystals, which rapidly developed into the field of X-ray crystallography of minerals and other crystals.

In *the geometrical optics of X-ray diffraction* the diffracting crystal is described as a set of parallel planes of atom layers separated by a constant distance d, which is called the *lattice plane spacing*. The X-rays are modeled by using conventional ray optics, assuming partial reflection of the X-rays of the incident plane wave from the atom planes. Like any two distinct lines in the three dimensional space, the incident and diffracted X-ray beams determine a plane, which is called *the diffraction plane*. Depending on the geometrical distance, the diffracted X-rays either strengthen or dampen when they interact with each other by interference. Then, Bragg's law of diffraction [8]

$$n\lambda = 2d \sin \theta \qquad (2.1)$$

is a direct consequence of the geometrical ray optics, and the requisite path difference enabling the constructive interference between the diffracted X-rays, as shown in the drawing of Fig. 2.1. The geometrical path differences in Bragg diffraction depend only on the lattice spacing d and diffraction angle θ. Therefore, Bragg's law is usually used for determining the atomic spacing d from the known X-ray wavelength λ and the Bragg angle θ, which is half of the measured diffraction angle 2θ.

The X-ray diffractometry (XRD) in Publications II, III, V, and IX was made with Philips X'Pert Pro diffractometer using normal resolution and high-resolution geometries. The X'Pert Pro diffractometer utilizes the characteristic radiation of the K absorption edge of the copper target inside the X-ray tube. When bombarded with electrons having 10–50 keV of kinetic energy, the copper target releases
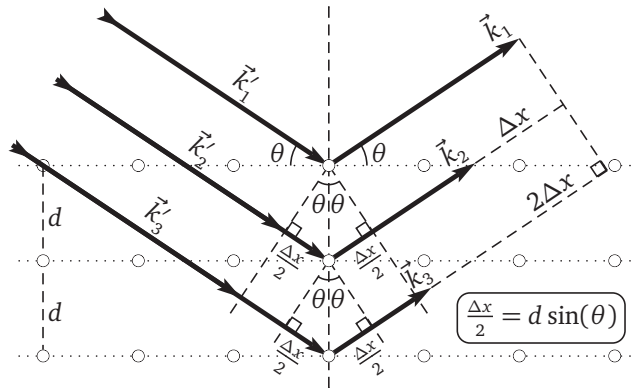
Figure 2.1: The geometrical optics of the Bragg X-ray diffraction from lattice planes with spacing d. The diffraction plane coincides the plane of the drawing. The incident $\vec{k}'_n$ and the diffracted $\vec{k}_n$ X-ray vectors of the respective plane waves have a path difference that is an integer multiple of Δx. Thus, $\Delta x = 2d\sin(\theta)$ must equal $n\lambda$ for some positive integer n in order to constructive interference to be possible.

X-ray radiation, which has three main components, the Cu-K$_{\alpha 1}$, Cu-K$_{\alpha 2}$ and Cu-K$_\beta$ characteristic X-ray peaks. The normal-resolution mode of the diffractometer has a nickel plate for filtering out the Cu-K$_\beta$ X-ray radiation, so that both of the Cu-K$_\alpha$ maxima remain in the X-ray spectrum. In the high-resolution mode the four-crystal Ge-220 monochromator blocks everything but the Cu-K$_{\alpha 1}$ radiation in order to achieve the maximum spectral resolution.

2.1.1 High-Resolution X-ray Diffractometry

High-resolution X-ray diffractometry (HR-XRD) can be used for accurate determination of the lattice parameters and the crystal quality of semiconductor crystals, if the normal-resolution mode of a diffractometer is not adequate. The X'Pert Pro diffractometer, which was used for collecting the HR-XRD data of Publications II, III, V, and IX, has a four-crystal Ge-220 monochromator for maximum spectral and spatial accuracy of the incident X-ray beam. After the X-rays pass through the monochromator, they diffract from the sample surface. Before the X-rays reach the point detector, they must be once more diffracted at the analyzer crystal, which improves the angular detection accuracy. Together the monochro-
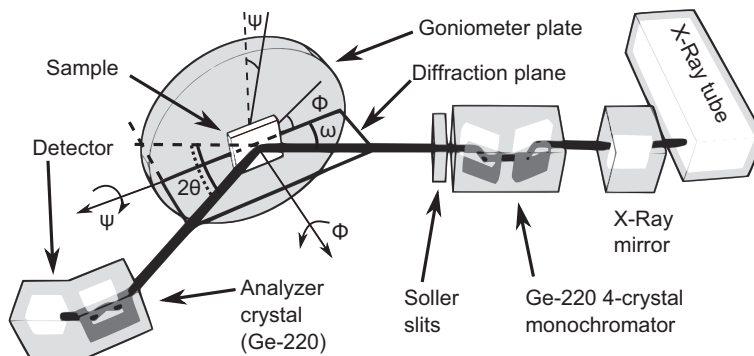
Figure 2.2: A schematic drawing of a HR-XRD setup showing the angles adjustable with the goniometer, i.e. diffraction angle 2θ, incident X-ray angle ω, azimuthal sample rotation angle ϕ, and the tilt angle ψ.

mator crystals, the sample and the analyzer crystal are called *the triple-axis system*, which enables an angular resolution of about 12 arcseconds for the X'Pert Pro. Figure 2.2 shows a schematic representation of the triple-axis HR-XRD setup utilized in data collection for Publications II, III, V, and IX.

An able X-ray diffractometer has a system of goniometers that can independently rotate the sample crystal about the incident X-ray angle ω axis, the azimuthal sample rotation angle ϕ axis, and the tilt angle ψ axis. The detector can also be rotated about an axis perpendicular to the diffraction plane, so that the detector angle corresponding to the diffraction angle 2θ may be arbitrarily chosen. Probably the most common measurement type for a traditional XRD system is *the rocking curve* scan, which is performed by increasing ω while keeping the detector at the center of the expected diffraction angle $2\theta_{hkl}$. The rocking curve scan yields information about the orientation variation of the scanned crystal planes related to the diffraction hkl within the diffraction plane. Another common measurement, especially for HR-XRD, is the ω–2θ scan, where ω and θ are increased by equal amounts during the scan, which makes the diffraction angle 2θ to change with twice the angular velocity in respect to the incident X-ray angle ω. Before the ω–2θ scan can proceed, the angles ϕ and ψ, as well as the offset angle between ω and θ should be aligned into suitable starting positions, usually by finding the highest possible detected X-ray intensity peak by performing test scans for each of the angular axes. Even though ω and 2θ are moved, the offset between ω and θ, as well the angles ϕ and ψ are kept constant during the scan.

After the initialization has been completed, i.e. the X-ray peak has been found, the angular space around the peak is scanned. This procedure yields an X-ray diffraction curve, which reveals information about the lattice strain and orientation with respect to the lattice planes corresponding to the diffraction indices *hkl* of the scan.

The good angular accuracy of the HR-XRD also necessitates excellent crystal quality of the measured samples, because the four-crystal monochromator reduces the incident X-ray intensity to about one tenth of the normal-resolution mode intensity to begin with, and furthermore the HR-XRD geometry is far more sensitive to any imperfections in the crystal lattice of the sample. Thus, in all but the highest-quality crystals the normal-resolution XRD mode has to be used in order to record enough diffracted intensity under practical measurement time frames. Normal-resolution XRD was used extensively in Publications III and IX in order to collect data from small crystallites having relatively imperfect lattices and small volumes.

2.1.2 Real and Reciprocal Lattices

Because the crystal lattice can be constructed by repeating copies of the unit cells without leaving any empty space between the adjacent cells, the positions of the cell corners are always reachable with integer multiples of the unit cell edge lengths, if the path is traveled along the cell edges. Thus, it is straightforward to define *lattice unit vectors* $\vec{a}_1$, $\vec{a}_2$, and $\vec{a}_3$ spawning from a single corner of the unit cell, and having the length of and extending along the three corresponding unit cell edges. Using the lattice unit vectors as a basis, the corners of all the cells in the lattice fall on integer coordinates $\vec{r} = u\vec{a}_1 + v\vec{a}_2 + w\vec{a}_3$, where u, v, and w are integers. Thus, the unit vectors $\vec{a}_1$, $\vec{a}_2$, and $\vec{a}_3$ of a crystal lattice are defined by the translational symmetry of the lattice itself, and they must be linearly independent vectors, which could translate the geometrical lattice onto itself in the three-dimensional space.

When X-ray diffraction problems are analyzed, it is convenient to define *reciprocal lattice* unit vectors $\vec{q}_1$, $\vec{q}_2$, and $\vec{q}_3$, in addition to the real-space lattice unit vectors. The definitions of the reciprocal lattice unit vectors are based on the real-space unit vectors $\vec{a}_1$, $\vec{a}_2$, and $\vec{a}_3$ of the crystal lattice, and the reciprocal unit vectors

can be written as [9, p. 491]

$$\vec{q}_1 = \frac{1}{V_u} \left(\vec{a}_2 \times \vec{a}_3 \right)$$

$$\vec{q}_2 = \frac{1}{V_u} \left(\vec{a}_3 \times \vec{a}_1 \right) \tag{2.2}$$

$$\vec{q}_3 = \frac{1}{V_u} \left(\vec{a}_1 \times \vec{a}_2 \right),$$

where the unit cell volume $V_u = \vec{a}_1 \cdot (\vec{a}_2 \times \vec{a}_3)$. The reciprocal rule that $\vec{a}_n \cdot \vec{q}_m = 1$ if and only if $n = m$, and zero otherwise, follows directly from the definition (2.2). For the cubic lattices the reciprocal unit vectors are parallel to the real-space lattice unit vectors, but the same is not necessarily true for other types of lattices. For example, the hexagonal lattices have $\vec{a}_n$ and $\vec{b}_n$ parallel only for $n = 3$, but not for $n = 1$ or $n = 2$.

2.1.3 Miller Indices and Lattice Spacing

The lattice spacing d, which is measurable by XRD, can be connected to the lattice constant a of the crystal by equations based on the lattice geometry. These equations contain integers describing the orientation of a plane within a lattice. The integers are called *Miller indices*, and they are related to the reciprocal lattice unit vectors $\vec{q}_1$, $\vec{q}_2$, and $\vec{q}_3$. Miller indices can be used with the parentheses for the crystal planes (hkl), with the braces for the symmetrically equivalent set of the crystal planes $\{hkl\}$, with the square brackets for the crystal directions $[hkl]$, with the angle brackets for the symmetrically equivalent set of the crystal directions $\langle hkl \rangle$, and without brackets for the diffractions hkl. Then, Miller indices (hkl) describe a crystal plane S in the lattice by its normal vector $\vec{s}$ with a simple relation $\vec{s} = h\vec{q}_1 + k\vec{q}_2 + l\vec{q}_3$ using the reciprocal vectors. For the cubic lattices, the connection between Miller indices of a diffraction hkl, lattice spacings d and lattice constant a depend on the lattice geometry by

$$d = \frac{a}{\sqrt{h^2 + k^2 + l^2}}, \quad a = |\vec{a}_1| = |\vec{a}_2| = |\vec{a}_3|. \tag{2.3}$$

The hexagonal lattice has two distinct lattice constants a and c, of which a is the hexagon edge length and c is the spacing between the hexagonal sheets. The

equation for lattice spacing d in hexagonal lattice is

$$\frac{1}{d^2} = \frac{1}{a^2}\left[\frac{4}{3}(h^2 + hk + k^2) + \frac{l^2 a^2}{c^2}\right], \quad a = |\vec{a}_1| = |\vec{a}_2|, \quad c = |\vec{a}_3|. \quad (2.4)$$

Because the Miller indices hkl in the X-ray diffractometry of the inorganic semiconductor crystals are all bound to be small integers, they can be often determined if the lattice spacing d is known exactly, and the lattice constant a is known approximately. This analysis was done for the InP pyramidical hillocks in Publication IX by assuming that the lattice constant a would be fairly close to that of Ge. The aim was to ascertain that the measured diffraction peaks were from the {111} crystal planes of the InP pyramidical hillocks, and not from some other unidentified crystal planes {hkl}.

2.1.4 Structure Factor and Forbidden Reflections

Crystals having the simple cubic lattice structure can diffract X-rays from any of their crystal planes for which the Bragg condition is met. However, this is not generally true for all of the lattice structures, most of which have so-called *forbidden reflections*, which do not produce diffracted intensity even if the Bragg condition is met. The intensity of the diffracted X-ray beam depends on a property of the crystal called *the structure factor* $\mathcal{F}_{hkl}$. The amplitude of the electric field of the X-ray beam diffracted from a crystal is proportional to $|\mathcal{F}_{hkl}|$, so that the diffracted X-ray beam intensity is proportional to $|\mathcal{F}_{hkl}|^2$ in Bragg diffraction [10, p. 29]. The structure factor is defined by

$$\begin{aligned}
\mathcal{F}_{hkl} &= \sum_{n=1}^{N_u} f_n e^{\frac{2\pi i}{\lambda}\left(\vec{k}-\vec{k}'\right)\cdot\vec{r}_n} \\
&= \sum_{n=1}^{N_u} f_n e^{2\pi i\left(h\vec{q}_1 + k\vec{q}_2 + l\vec{q}_3\right)\cdot\left(u_n\vec{a}_1 + v_n\vec{a}_2 + w_n\vec{a}_3\right)} \quad (2.5) \\
&= \sum_{n=1}^{N_u} f_n e^{2\pi i\left(hu_n + kv_n + lw_n\right)},
\end{aligned}$$

where hkl are the Miller indices of the diffraction, f_n are *the atomic scattering factors*, and u_n, v_n, and w_n are the fractional coordinates of each of the N_u atoms in the crystal's unit cell [9, p. 117]. The fractional coordinates range from zero to unity, and the atomic scattering factors f_n depend on the species of the atom n in the unit cell. In a given lattice, the terms of the sum in equation (2.5) may

Table 2.1: The squared structure factors of the diamond, zincblende [10, p. 34], and wurtzite lattices. The wurtzite structure factors are calculated using the data from [10] and [12]. In the Miller indice rules, n and m are any integers fulfilling the conditions, and zero is considered to be an even number. The atomic scattering factors f_A and f_B refer to the two constituent atom species in the zincblende and wurtzite lattices.

Lattice	Rule for the Miller indices hkl	Squared structure factor $\mathcal{F}_{hkl}^2$	Remarks
Diamond	$h+k+l = 4n$, all even	$64f^2$	Largest
	$h+k+l \neq 4n$, all even	0	Forbidden
	hkl all odd	$32f^2$	
	hkl mixed	0	Forbidden
Zincblende	$h+k+l = 4n$, all even	$16(f_A+f_B)^2$	Largest
	$h+k+l \neq 4n$, all even	$16(f_A-f_B)^2$	Weak
	hkl all odd	$16(f_A^2+f_B^2)$	
	hkl mixed	0	Forbidden
Wurtzite	$h+2k = 3n, l = 8m$	$4(f_A+f_B)^2$	Largest
	$h+2k = 3n, l = 4m+2$	$4(f_A^2+f_B^2)$	
	$h+2k = 3n, l = 8m+4$	$4(f_A-f_B)^2$	Weak
	$h+2k = 3n, l$ odd	0	Forbidden
	$h+2k \neq 3n, l = 8m$	$(f_A+f_B)^2$	
	$h+2k \neq 3n, l = 4m+2$	$f_A^2+f_B^2$	
	$h+2k \neq 3n, l = 8m+4$	$(f_A-f_B)^2$	Weak
	$h+2k \neq 3n, l = 8m\pm1$	$3(f_A^2 - \frac{1}{\sqrt{2}}f_Af_B + f_B^2)$	
	$h+2k \neq 3n, l = 8m+4\pm1$	$3(f_A^2 + \frac{1}{\sqrt{2}}f_Af_B + f_B^2)$	

cancel each other out for some diffractions hkl, in which case $F_{hkl} = 0$. Thus, the diffraction intensity would be zero, and no diffraction would actually occur. Such diffractions hkl are called *forbidden reflections*, because there would be no diffracted intensity even if the Bragg condition (2.1) was fulfilled for the particular diffraction. The exact values for the squared structure factors applicable to the materials studied in this work are listed in Table 2.1.

Silicon (Publication III) and germanium (Publications II, IV and IX) have the diamond lattice structures, for which all of the diffractions are forbidden expect those either having all the Miller indices hkl odd, or alternatively, all hkl even and their sum divisible by four. Almost the same rule for forbidden reflections is valid for the zincblende lattice structure of III-V compound semiconductors InAs, InP, GaAs and GaInP, which were topographed in Publications I, II, III, IV, V, VII, VIII

and IX. However, in addition to the diamond lattice reflections, the zincblende lattice shows weak diffractions for reflections having all hkl even and $h+k+l+2$ divisible by four [9]. Figure 1.1 a) shows the atom positions in zincblende lattice unit cell. GaN studied in Publication VI has the hexagonal wurtzite lattice, a schematic drawing of which is in Fig. 1.1 b). The hexagonal cell is not the unit cell of the wurtzite lattice [11], but helps visualizing the hexagonal symmetry of the lattice. As shown in Table 2.1, all reflections are allowed in the wurtzite lattice, except those that have $h + 2k$ divisible by 3 and l odd. However, those of the allowed reflections that have $l = 8m + 4$ for some integer m are weak, i.e. they would be forbidden if the lattice consisted of only one atom species.

2.1.5 Ewald Sphere

Figure 2.3 shows a schematic drawing of the cross-section of *the Ewald sphere* for 040 diffraction, which is a reflection commonly used in XRD measurements. The Ewald sphere is constructed in the reciprocal space, and it is centered at the origin of the equal-length incident $\vec{k}'$ and diffracted $\vec{k}$ reciprocal X-ray beam vectors. The diffraction vector $\vec{g} = \vec{k} - \vec{k}'$ connects the reciprocal origo 000 to the reciprocal lattice point hkl of the diffraction, and both of the diffraction vector endpoints lie on the surface of the Ewald sphere. In crystallography, the lengths of the X-ray beam vectors and thus the radius of the Ewald sphere are usually chosen to be $|\vec{k}| = |\vec{k}'| = 1/\lambda$, i.e. the reciprocal of the X-ray wavelength, as is the case here, but occasionally it is scaled by a factor of 2π for mathematical convenience [13, 78]. In order to X-ray diffraction to be possible, the diffraction vector $\vec{g}$ endpoints must coincide with reciprocal space points having integer coordinates, but there is no such requirement for the Ewald sphere center. Because $|\vec{k}| = |\vec{k}'|$, the vectors $\vec{k}$, $\vec{k}'$, and $\vec{g}$ form an isosceles triangle inside the Ewald sphere. Using the Ewald sphere construction in Fig. 2.3, the equation for the X-ray diffraction simplifies to

$$\vec{k} - \vec{k}' = h\vec{q}_1 + k\vec{q}_2 + l\vec{q}_3, \tag{2.6}$$

from which the Bragg's law (2.1) can be directly derived.

The Ewald sphere construction is particularly useful in the wide-spectrum SR-XRT case, as shown in the schematic drawing of Fig. 2.4, where several diffractions $\vec{g}_n$ ($n = 1$ to 8) with distinct X-ray wavelengths λ_n correspond to the Ewald spheres having different radii. The number of the possible diffractions is limited by the width of the available spectrum, which is indicated by the limiting wavelengths
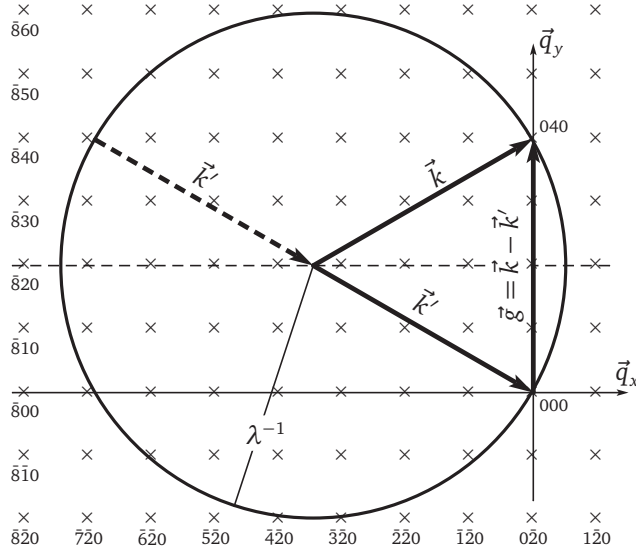
Figure 2.3: Schematic drawing of $l = 0$ cross-section of the Ewald sphere in the reciprocal space. The drawing corresponds to the single-wavelength XRD geometry with 040 diffraction from a cubic crystal. The diffraction vector $\vec{g}$ is determined by the incident X-ray vector $\vec{k}'$ and diffracted X-ray vector $\vec{k}$ so that $\vec{g} = \vec{k} - \vec{k}'$ and $|\vec{k}| = |\vec{k}'| = \lambda^{-1}$. Dashed vector $\vec{k}'$ and the dashed horizontal line represent the incident X-ray beam and the crystal surface assumed to be parallel to the diffracting planes, i.e. the real-space (xz-plane), in respect to the diffracted beam $\vec{k}$.

λ_a and λ_b in the figure. In the wide-spectrum Laue case the crystal diffracts all of the allowed diffractions that have their reciprocal lattice points hkl between the limiting spherical surfaces, only some of which are shown in Fig. 2.4. The parallel diffraction vectors $\vec{g}_n$ of the 200, 400, 600, and 800 diffractions also have parallel $\vec{k}_n$-vectors for $n = 1$ to 4, which means that the diffracted beams $h00$ overlap and go into exactly the same direction. However, diffractions 200 and 400 are either forbidden or weak in the diamond and zincblende lattices, respectively, so that the total intensity of the diffractions $h00$ may mainly consist of the diffractions 400 and 800. The $hh0$ type reflections 220, 440, and 660 are similarly headed to common direction, but none of them are forbidden in the diamond and zincblende lattices. The diffractions $\vec{g}_n$ ($n = 1$ to 7) are *backward-diffracted*, i.e. the angle between vectors $\vec{k}'_n$ and $\vec{k}_n$ is larger than 90°. The only *forward-diffracted* beam shown in Fig. 2.4 is the forbidden reflection 140, for which the angle between $\vec{k}'_8$ and $\vec{k}_8$ is clearly less than 90°.
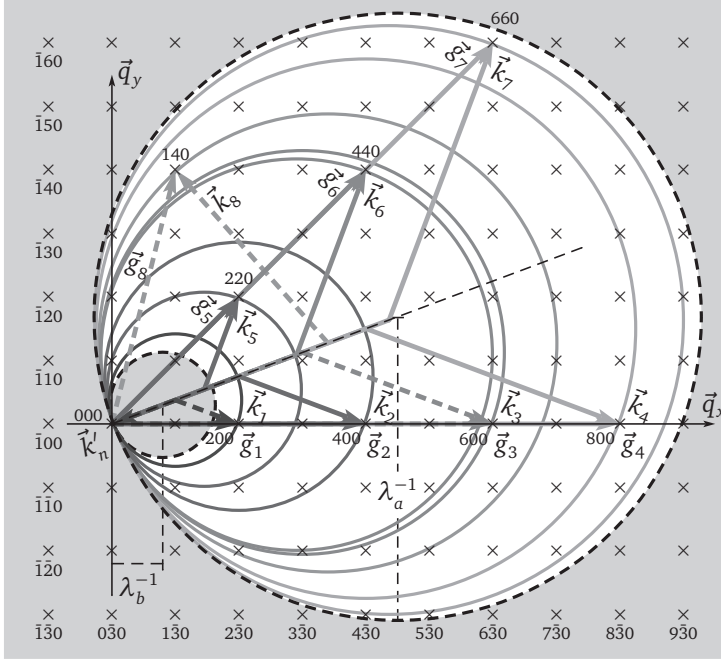
Figure 2.4: Schematic drawing of $l = 0$ cross-section of the Ewald spheres in the reciprocal space. The drawing corresponds to the Laue geometry with continuous X-ray spectrum with wavelengths between λ_a and λ_b, which is applicable for the synchrotron X-ray topography case. Each of the diffraction vectors $\vec{g}_n$ are determined by the parallel incident X-ray vectors $\vec{k}'_n$ of wavelength λ_n and the diffracted X-ray vectors $\vec{k}_n$ so that $\vec{g}_n = \vec{k}_n - \vec{k}'_n$. The diffractions plotted with dashed lines are forbidden in the diamond lattice, and either forbidden (140) or weak (200 and 600) in the zincblende lattice.

2.1.6 Reciprocal Space Maps

Reciprocal space maps (RSM) of Publications II and IX were measured in the HR-XRD-mode of the diffractometer, even though they could have been measured in XRD-mode, albeit with considerably worse accuracy. RSMs are measured by scanning a series of ω–2θ curves, where the offset between the incident X-ray angle ω and the Bragg angle θ is varied between the scans. Thus, any small variations in the lattice constant or lattice orientation of the sample crystal produce measurable intensity for their respective ω, θ values. These intensity values in
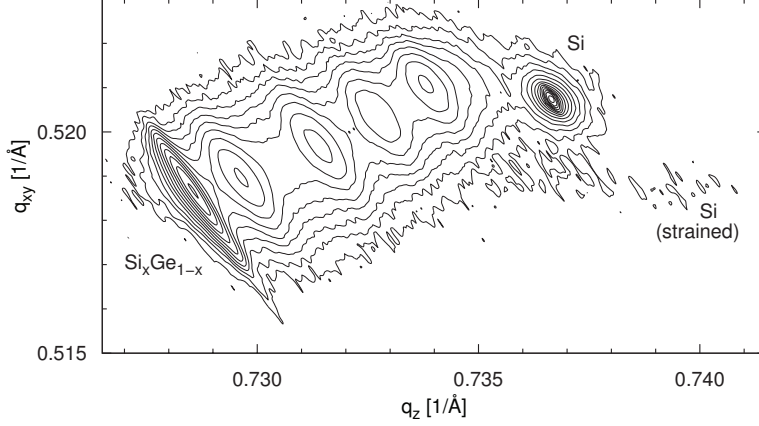
Figure 2.5: Asymmetrical 224 **reciprocal space map of strained Si on relaxed SiGe buffer on Si substrate measured by the author, and previously published in [14]. Reciprocal coordinates** q_{xy} **and** q_z **correspond to components** 220 **and** 004, **respectively.**

ω, θ space are further mapped to reciprocal space by assuming that changes in lattice orientation are negligible, i.e. that all intensity changes in ω and θ are related to changes in lattice constants along principal crystal axes rather than in lattice orientation. Provided that the assumption is valid, it is possible to calculate the diffracted intensity on the Ewald sphere in the reciprocal space, and map the data to reciprocal space coordinates q_x, q_y, and q_z, which correspond to the reciprocal unit vectors $\vec{q}_1$, $\vec{q}_2$, and $\vec{q}_3$ of the cubic lattice. The RSM thus shows the strain-induced variations in the lattice constants along the reciprocal axes of the measured diffraction plane (hkl), where h, k, l are the Miller indices. In practice, the RSMs are measured either at a symmetrical diffraction geometry (e.g. 004 diffraction in the cubic lattices), or at an asymmetrical diffraction geometry (e.g 224 diffraction in the cubic lattices). The asymmetric geometry is beneficial if lattice relaxation is to be expected, because using an asymmetric geometry one of the reciprocal axes lies along the sample surface, i.e. on the relaxation direction. Figure 2.5 shows an asymmetrical 224 RSM measured from a sample having a 12 nm thick strained Si on relaxed SiGe buffer on Si substrate [14]. The RSM has two main diffraction peaks, these are produced by the Si substrate and the fully relaxed SiGe buffer. The faintly visible very thin strained Si layer is clearly completely strained with no relaxation, because it has the same q_{xy} coordinate as the SiGe layer it is grown on.

2.2   Synchrotron Radiation X-Ray Topography

2.2.1   Synchrotron Radiation

Synchrotrons produce wide spectrum of radiation by utilizing *Bremsstrahlung*, which is electromagnetic radiation produced by accelerating charged particles. In synchrotrons, electrons or positrons are accelerated to near light speed in vacuum and put into a large storage ring, where the direction of the charged particle beam is altered by *bending magnets*, so that the path of the charged particles forms a closed ring. Synchrotron radiation can be extracted and utilized by the bending magnets and *insertion devices*: wigglers or undulators. Figure 2.6 shows an illustration of a synchrotron radiation source, where bending magnets are used as X-ray sources at *the storage ring*. In the illustrated source there is a linear accelerator sourcing the synchrotron with fast charged particles, either electrons or positrons. The synchrotron further accelerates the charged particles, which are then transferred to the storage ring during *injection*. Injection of the charged particles into the storage ring may halt the normal operation of the synchrotron radiation source, because the orbits of the charged particles are disturbed and the quality of the beam collimation drops, and the beam shutters are usually closed for safety reasons. The charged particles continue to orbit the storage ring for a few hours, during which time their Bremsstrahlung at the bending magnets or insertion devices can be exploited as an X-ray source. When a path of fast electrons (or positrons) is turned in a bending magnet or an insertion device inside the synchrotron, an intense beam of wide-spectrum electromagnetic radiation emerges due to the normal component of the electron acceleration. If the particles are fast enough, the frequency of the photon radiation may reach the X-ray or γ-ray parts of the electromagnetic spectrum. The bending magnets of large synchrotrons produce wide electromagnetic spectra ranging from infrared radiation through light and ultraviolet UV radiation into X-rays, and consequently the radiation is called *wide-spectrum radiation* or *white beam radiation*.

Most of the synchrotron radiation X-ray topography (SR-XRT) experiments of Publications I–IX were made at the topography station F1 of the Hamburger Synchrotronstrahlungslabor am Deutsches Elektronen-Synchrotron (HASYLAB-DESY) in Hamburg [17], with the rest made at the topography beamline of Angstromquelle Karlsruhe (ANKA) at Forschungszentrum Karlsruhe [18, 19]. The DESY synchrotron radiation source is operated according to the principle outlined in the schematic illustration of Fig. 2.6. The X-ray photon flux Φ of a synchrotron is measured with its *spectral brightness*, which takes into account
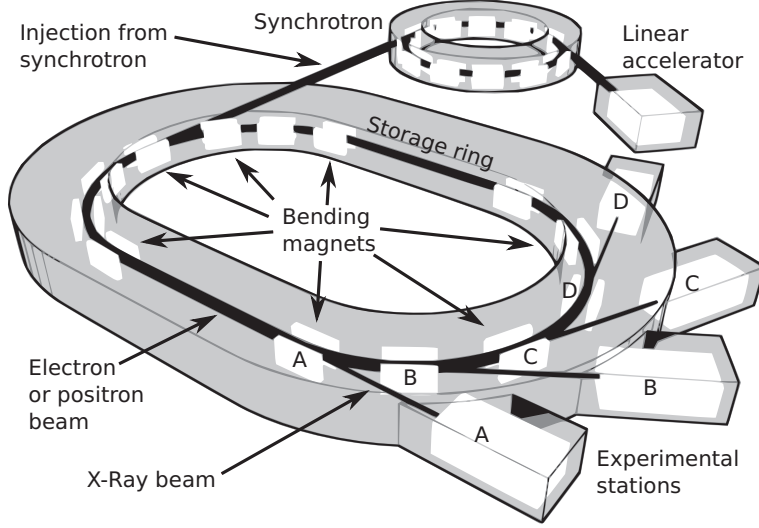
Figure 2.6: An illustration of a synchrotron radiation source with four of the bending magnets used as insertion devices A–D, each having corresponding experimental stations.

the synchrotron X-ray photon beam emittances ε_x and ε_y, and which has a unit photons/s $\times$ mm^{-2}mrad^{-2}(0.1 % Bandwidth)$^{-1}$ [20]. The spectral brightness of HASYLAB-DESY F1/Topography beamline at typical synchrotron storage ring beam current of 140 mA is shown in Fig. 2.7, where the maximum spectral brightness is $\approx 5 \times 10^{13}$ photons/s $\times$ mm^{-2}mrad^{-2}(0.1 % Bandwidth)$^{-1}$ at the critical photon energy 16 keV of the DORIS III storage ring bending magnets. Spectral brightnesses of modern 3rd-generation storage ring insertion devices are in the range of $10^{19} - 10^{22}$ photons/s$\times$mm^{-2}mrad^{-2}(0.1 % Bandwidth)$^{-1}$, which is too large a spectral brightness for X-ray topography.

The DORIS III synchrotron storage ring bending magnet spectral brightness curves in Fig. 2.7 are calculated from

$$\frac{d^2\mathcal{I}}{d\omega_s d\Omega_s} = \frac{q^2}{12\pi^3\epsilon_0 c}\left(\frac{\omega_s\rho}{c}\right)^2\left(\frac{1}{\gamma^2}+\vartheta^2\right)^2\left[K_{2/3}^2(\xi)+\frac{\vartheta^2}{1/\gamma^2+\vartheta^2}K_{1/3}^2(\xi)\right] \quad (2.7)$$

$$\xi = \frac{\omega_s\rho}{3c}\left(\frac{1}{\gamma^2}+\vartheta^2\right)^{3/2} \text{ and } \gamma = \frac{E}{m_0 c^2} \quad [21],\qquad (2.8)$$
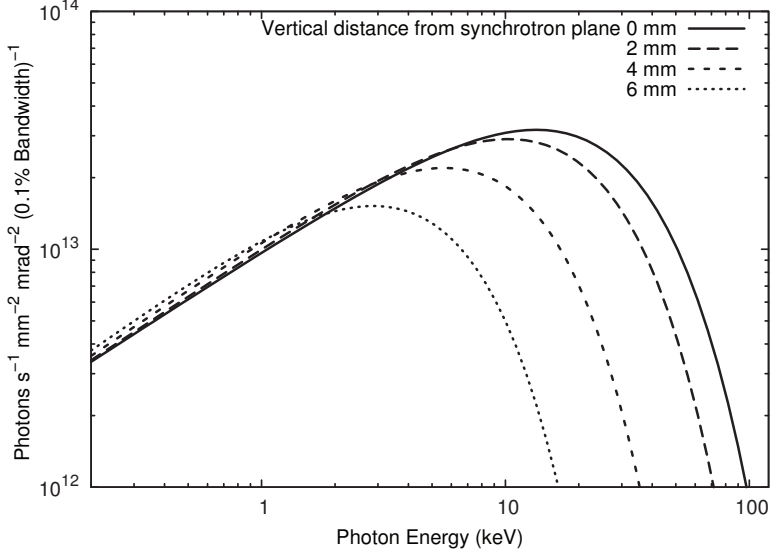
Figure 2.7: X-ray spectral brightnesses of DESY DORIS III bending magnet source at F1/Topography station on various vertical positions. The vertical distance is measured from the center of the synchrotron plane inside the Laue-camera positioned 37 m away from the source [15]. The positron current is 140 mA at 4.45 GeV positron energy. The curves are calculated from DESY parameters [16] using equations (2.7) and (2.8).

where $\mathcal{I}$ is the X-ray radiation energy per positron, ω_s the angular frequency of the X-rays, Ω_s the solid angle of the radiation cone, q the elementary charge, ϵ_0 the vacuum permittivity, c the speed of light in vacuum, γ the relativistic factor, ρ the instantaneous synchrotron orbit radius, ϑ the angle between the synchrotron plane and the X-rays, E the positron energy at DORIS III, and m_0 the positron rest mass. $K_{2/3}(\xi)$ and $K_{1/3}(\xi)$ are the modified Bessel functions. From the energy per bandwidth $d\mathcal{I}/d\omega_s$ it is possible to calculate the X-ray photon flux per 0.1 % bandwidth $\Phi = (10^{-3}/\hbar) \times (d\mathcal{I}/d\omega_s) \times (I_c/q)$, where I_c is the positron current of the synchrotron [22]. Finally, the spectral brightness can be calculated from the X-ray photon flux Φ by dividing it with the product of the horizontal and vertical photon beam emittances ε_x and ε_y, which are characteristic properties of a synchrotron [21].

2.2.2 Laue Patterns

If a crystal is exposed to the white beam radiation, the Bragg diffraction condition of equation (2.1) is fulfilled for all of the crystal planes (hkl) that are hit by the beam. The white beam spectrum contains, among others, the correct Bragg wavelength λ_{hkl} for the Bragg angle θ_{hkl} between any lattice plane (hkl) and the incident beam, so that an X-ray beam having a wavelength of λ_{hkl} is diffracted. Therefore, multiple diffracting beams having distinct wavelengths λ_{hkl} are produced by a single incident white beam. The diffracted X-ray beams diverge to various diffraction directions $\vec{g}$ depending on the lattice structure and orientation of the crystal. The geometrical projection of diffraction vector $\vec{g}$ end points on a plane is called the *Laue pattern* after the German physicist Max von Laue. Laue patterns can be experimentally produced by irradiating crystals, preferably monocrystals, and simultaneously exposing X-ray sensitive films or photographic plates to the diffracted X-ray beams. The first Laue patterns were recorded by M. Von Laue *et al* by utilizing the continuous part of the X-ray spectrum of an X-ray tube [5]. If the monocrystal is of sufficient quality, a Laue pattern is seen as a set of dark spots on the exposed film. The basis of the original Laue method has survived in scientific use to the present day, albeit only when used with the more powerful synchrotron X-ray sources. An individual spot in the Laue pattern is called *an X-ray topograph*. The topographs are roughly the same size as the cross-section of the incident beam, but the spots may be elongated for geometrical reasons. The positions of the topographs in a Laue pattern can be straightforwardly calculated using simple vector geometry by assuming mirror-like reflections from the crystal planes. By measuring the topograph positions on the film it is possible to determine the crystal orientation, and calculate the Bragg angles θ_{hkl} from the geometry, and then combine the lattice spacings from equations (2.3) or (2.4) with Bragg's law (2.1) to find the X-ray wavelengths and energies of each topograph. Figure 2.8 shows a Laue pattern of topographs recorded by the author using synchrotron radiation. The Laue pattern was indexed with a computer program, which calculates the X-ray energies and Miller indices hkl of the topographs by using the explained method.

For a given X-ray wavelength fulfilling the Bragg diffraction condition, there may also be other X-ray wavelengths diffracting at exactly the same Laue geometry. These distinct diffractions occur at *harmonic X-ray frequencies*, which are integer multiples of the *the base frequency*. The Miller indices corresponding to the harmonic frequencies are also integer multiplies of the smallest possible choice of the Miller indices describing the diffracting crystal plane. The occurence of harmonic diffractions in cubic reciprocal space is shown schematically in Fig. 2.4,
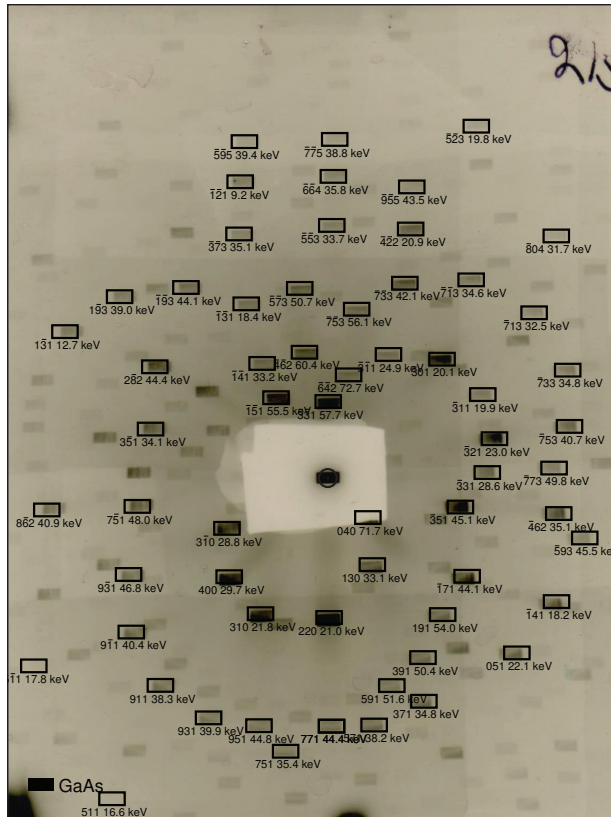
Figure 2.8: Laue pattern of large-area transmission topographs recorded from a GaAs crystal. The sample was rotated 8.5° about the horizontal axis by tilting the sample holder. Simulated Laue spots are overlaid onto the pattern together with the related Miller indices of the smallest allowed diffractions. Also, the corresponding diffraction energies are calculated. (Recorded in HASYLAB, Feb 2007, film 215)

where some of the harmonic diffractions of type $h00$ and $hk0$ ($h = k$) are shown. In practice, a topograph recorded on X-ray film may consist of overlapping images produced by subsequent harmonic X-ray frequencies, but in some cases only one harmonic frequency is dominant and produces a strictly monochromatic topograph. The transmission topographs recorded from {331} InAs crystal planes and printed in Publication I are such monochromatic topographs.

2.2.3 Topographs

There are several possible detection techniques available for Laue patterns and the topographs: scintillation screen optics, storage phosphor image plate systems, structured scintillation screen optics, directly excited charge-coupled devices (CCD), and specially crafted photocathode video cameras [23, 24]. The spatial resolution of X-ray sensitive high-resolution films $r_F \ll 1\,\mu$m has been superior to the other detection techniques having $r_0 > 1\,\mu$m [23], which has been the driving reason to only use high-resolution film as a synchrotron radiation X-ray topography (SR-XRT) detector. However, recent developments in scintillator detector cameras have produced topographs comparable to those on high-resolution film [25]. Thus, high-quality SR-XRT topographs are generally either recorded on high-resolution X-ray film [17, 26], or produced with a combination of a scintillator and a digital CCD detector [25]. All topographs in Publications I–IX were recorded on high-resolution Slavich VRP-M holographic X-ray sensitive films, and subsequently enlarged with optical microscope.

Provided that the resolution of the detector is adequate, the geometric resolution depends on the source-to-sample distance L, the sample-to-detector distance x, and the size of the source. For the DORIS III synchrotron bending magnets the standard deviations of spatial distributions around the central positron orbit are $\sigma_x = 1.0$ mm and $\sigma_z = 0.3$ mm, which corresponds to FWHM sizes $\Sigma_x = 2.4$ mm and $\Sigma_z = 0.71$ mm. Thus, the horizontal and vertical geometrical resolutions, both defined by $r = \frac{x}{L}\Sigma$, are $r_x \approx 4\,\mu$m and $r_z \approx 1\,\mu$m for the DORIS III bending magnet at the F1 Topography station. The F1 Topography station sample-to-detector and source-to-sample distances are $x \approx 60$ mm and $L \approx 37$ m, respectively [15].

The high irradiance of the synchrotron radiation allows for exposure times of minutes or seconds [27], which is far shorter than the several days or hours required in conventional X-ray topography on high-resolution holographic X-ray sensitive film [28]. Another advantage of synchrotron radiation is the small spatial size of the source and very high degree of collimation of the X-ray beam. The high degree of collimation enables the use of long source-to-sample distances without significant angular divergence or decrease in X-ray intensity. The source-to-sample distances in synchrotron topography can be tens of meters, which can be exploited by increasing the sample-to-film distance to over 10 cm without loss of geometrical resolution affecting the overall resolution. Resolution of X-ray tube topography is always limited by the geometrical resolution, which neces-
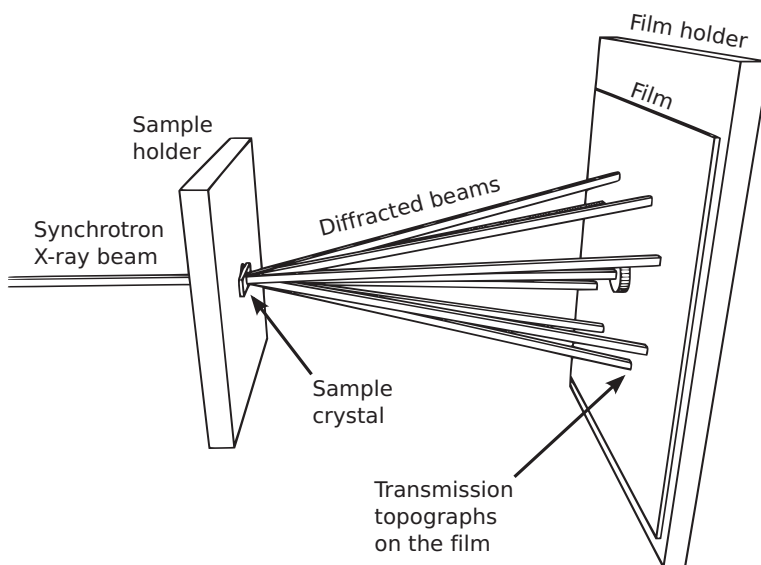
Figure 2.9: A schematic representation of a typical setup used in the synchrotron radiation X-ray transmission topography geometry.

sitates sample-to-film distances of less than 1 cm. Thus, complicated sample mounting setups with cryogenic vacuum devices or other apparatuses are far easier to implement in SR-XRT than in conventional topography.

2.2.4 Transmission Topography

The few distinct measurement configurations available in SR-XRT are mainly classified by the measurement geometry. In transmission topography the film is put behind the sample crystal, so that all the X-ray radiation recorded on the film must have traveled through the sample. Thus, the X-ray penetration depth in transmission topography is equal to the thickness of the sample, and therefore transmission topography provides information about the full volume of the imaged area within the sample. Figure 2.9 is a schematic representation of a typical transmission topography setup. The setup consists of a sample holder with an X-ray hole, a sample crystal, a film holder and the X-ray film. In front of the film there is a beam stopper made of lead for preventing potential damage to the
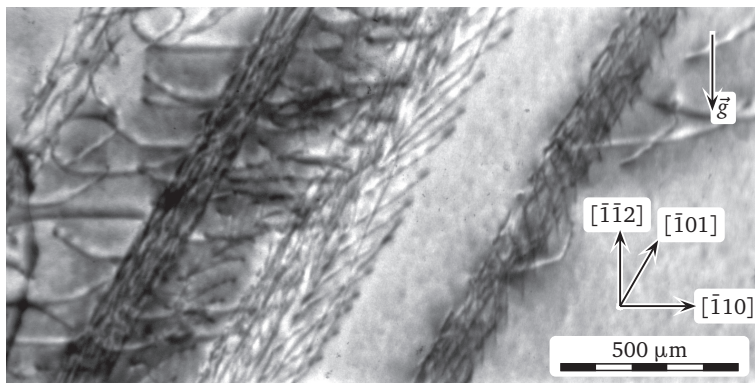
Figure 2.10: $11\bar{3}$ **large-area transmission topograph of a highly As-doped silicon wafer showing dislocation belts and threading dislocations. Diffraction vector $\vec{g}$ projection and some crystal directions along the sample surface are indicated.**

film inflicted by the direct beam. The X-rays travel through the sample, wherein some of the X-ray wavelengths are diffracted into various directions and form the topographs onto the film. Because the diffractions happen at specific low-index atom planes of the crystal, the distribution of the topographs reflects the same symmetry that the crystal has. However, due to the geometrical projection of the diffracted directions, it is not always easy to immediately recognize what kind of crystal geometry a given Laue picture has. Figure 2.8 shows a Laue pattern of large-area transmission topographs recorded from a GaAs crystal, with simulated Laue-spots, Miller's indices, and X-ray energies overlaid on top of the image.

The transmission geometry is further subdivided into large-area transmission topography and transmission section topography. The beam size in *large-area transmission topography* is several square millimeters, and the shape of the beam is often close to a square or a rectangle, even though circular, elliptical or other beam shapes can readily be used. Large-area transmission topography is especially suited for studying crystal wafers of electronic materials known to have only few dislocations (i.e. $0\ldots10^4$ cm^{-2}, such as GaAs substrates [29, 30], and InSb substrates [31], and InAs substrates (Publication I). The advantage of the large-area transmission SR-XRT geometry are the facts that it is nondestructive to the samples, and that it can, in principle, image all the dislocations inside the bulk of the sample. Figure 2.10 shows a large-area transmission topograph displaying numerous dislocations, which are almost all aligned to belts bor-
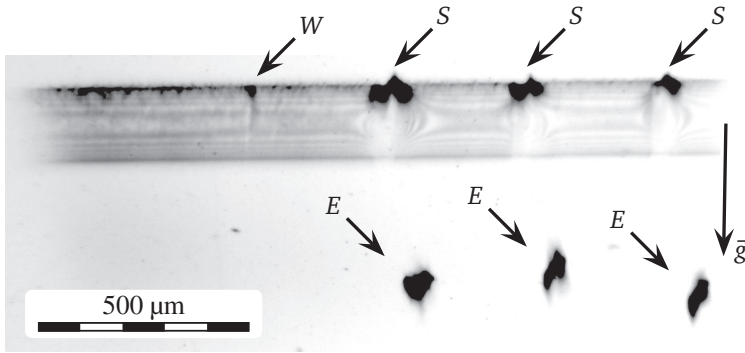
Figure 2.11: 311 **transmission section topograph of an InP ELO layer on Si sample of Publication III. The substrate lattice displays clear Pendellösung fringes. Strain fields in the Si substrate** S**, ELO layers** E**, an empty growth window** W**, and diffraction vector** $\vec{g}$ **projection are indicated.**

dered by {110} crystal planes. Due to the relatively low dislocation density of $\approx 5 \times 10^3$ dislocations/cm² and almost macroscopic size of the ordered structures of dislocations in the sample, it would be almost impossible to discover the belt structure with any other method than large-area SR-XRT.

In *the transmission section topography* the cross-section of the X-ray beam is confined to an almost linear shape by inserting a narrow slit in front of the beam. Notwithstanding the addition of the slit, the geometry in transmission section topography is exactly the same as in large-area transmission topography. The horizontal width of the beam can be several millimeters, but the vertical beam thickness is limited to few tens of micrometers. The incident X-rays interact with the crystal only within a narrow section of the sample due to the shape of the incident beam. The reduction of the beam area also significantly reduces the total diffracted X-ray energy, so that the exposure time required in transmission section X-ray topography for a given sample is roughly tens of times longer than the same sample would require in large-area geometry. Transmission section SR-XRT geometry was used in Publications III, VI, VII and IX. Specifically, section topography was used to study the strain fields induced by the epitaxial features into the Si and Ge substrate wafers In Publications III and IX, respectively. Figure 2.11 shows a 311 transmission section topograph of an InP ELO on Si sample of Publication III. The topograph shows clear Pendellösung fringes in the Si substrate, but the fringes are deformed around the ELO growth windows due to the large
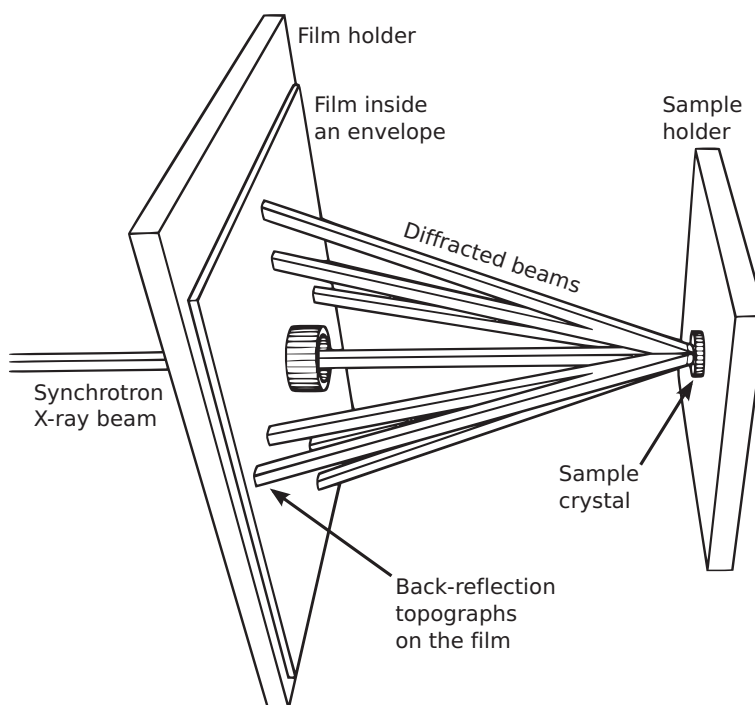
Figure 2.12: A schematic drawing of the setup used in synchrotron radiation X-ray back-reflection topography geometry.

strain fields caused by the ELO structures. Similar strain field effects studied by transmission section SR-XRT have been reported for metallization-induced strain [32, 33], and for the strain induced by laser micro-machining [34]. Publications VI and VII use transmission section SR-XRT for studying the epitaxial layer quality, GaN on sapphire and doped GaAs on GaAs, respectively.

2.2.5   Back-reflection Topography

Back-reflection geometry allows the recording of the X-ray reflections that are diffracted back from the sample surface (Fig. 2.12). In back-reflection SR-XRT the majority of diffracted X-rays do not penetrate the sample deeper than few

tens of micrometers. The downside of large-area back-reflection topography is an undesired background intensity on the topograph, which is produced by *X-ray fluorescence* emitted from the sample surface. Generally, heavier elements produce more X-ray fluorescence. The total amount of the background fluorescence is also proportional to the total radiant power of the incoming X-rays hitting the crystal surface, which often limits the practical beam size to 1×1 mm^2 or less.

The average X-ray penetration depth of back-reflection SR-XRT depends on the material and orientation of the crystal, the diffraction vector $\vec{g}$ and the Miller indices hkl. The X-ray intensity I in the crystal decreases exponentially by

$$I = I_0 \exp{-\mu_0 z}, \tag{2.9}$$

where I_0 is the original X-ray intensity, μ_0 is the average linear attenuation coefficient of the material at X-ray wavelength λ_{hkl}, and z is the depth. The back-reflected X-ray intensity of a topograph recorded from the depth of *the attenuation length* $\zeta = 1/\mu_0$ is less than $I_0 \exp(-2\mu_0\zeta) = I_0 \exp(-2) = 0.135 \times I_0$, i.e. 13.5 % of the intensity diffracted from the immediate surface. The attenuation length ζ is therefore a reasonable practical limit for the depth beyond which no significant contrast will be observed in the topograph, and can be considered the X-ray penetration depth in the back-reflection topography.

The average linear attenuation coefficient μ_0 depends heavily on the X-ray wavelength λ_{hkl} of the diffraction hkl. Because the Bragg angle θ can be straightforwardly measured from the likely-known crystal orientation and the diffraction vector $\vec{g}$ projection, it is feasible to calculate the Miller indices from the Laue pattern, and calculate the lattice spacings from (2.3) or (2.4) for known lattice constant a. Inserting the lattice spacing d and Bragg angle θ into Bragg's law (2.1), the X-ray wavelength λ_{hkl} and thus the average linear attenuation coefficient μ_0 and the penetration depth ζ can be calculated for any diffraction hkl. However, there are usually a number of allowed Miller indices hkl with integer proportions having the same diffraction geometry but distinct X-ray wavelengths, so that a back-reflection topograph may actually consist of a number of diffractions with different penetration depths. The outlined technique for determining the penetration depth of X-rays for given diffraction hkl was used in Publication I, where a back-reflection topograph was found to image mainly the epitaxial layer and not the substrate, due to the modest penetration depth.

Back-reflection section topography has the same main characteristics as the transmission section topography, i.e. the X-ray beam is confined to a narrow line hav-
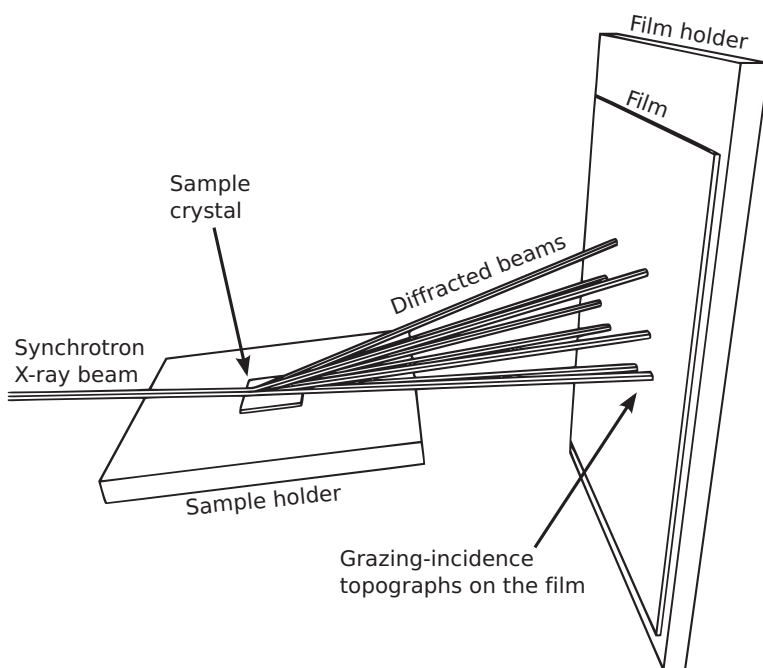
Figure 2.13: A schematic drawing of the setup used in synchrotron radiation X-ray grazing-incidence topography geometry.

ing a width of few tens of micrometers. Exposure times in the back-reflection section topography geometry are again about ten times longer than in the back-reflection large-area geometry. Back-reflection section topography was used in Publications II–IV. The section topographs recorded from ELO growth window openings of the samples of Publication III displayed high strain fields on the window edges, which would have been difficult to discover with other methods.

2.2.6 Grazing Incidence Topography

Grazing incidence X-ray topography is a variation of the back-reflection technique, but with the sample tilted so that the angle between the incident synchrotron X-ray beam and the sample surface is small. Figure 2.13 shows a schematic drawing of the sample and film positions relative to the X-ray beam in

grazing incidence topography geometry. Grazing-incidence geometry was used in Publication VII for imaging highly doped epitaxial GaAs layers on GaAs. A relatively large area on the sample surface can be irradiated even with a narrow beam, if the incident X-ray angle is less than 10°. However, if the incident X-ray angle ω is less than the critical angle $\alpha_c \approx \lambda (1/2\pi \mathcal{N} Z r_e)^{1/2}$, a total reflection occurs, in which case the X-rays typically penetrate the sample only about 50 Å before reflection [35, 36]. Critical angles are rather small for X-ray photons used in diffraction, *e.g.* silicon (100) $\alpha_c(\text{Si}) = 0.22°$ for 8 keV X-rays. In most cases it would not be reasonable to collect data from such a small volume of the sample as would result from 50 Å penetration depth. However, when the incident angle is small, yet larger than α_c, the recorded X-ray topographs still tend to image features from the immediate crystal surface. This is because the X-ray photons penetrate the crystal at an angle, albeit larger than α_c, but small enough to make the X-ray photon momentum vector surface normal component small. Typical X-ray penetration depth in grazing incidence geometry with $\omega > \alpha_c$ is in the order of few µm [36], and it can be increased by increasing ω, which makes grazing incidence geometry with $\alpha_c < \omega < 10°$ a practical method for SR-XRT.

3 Defect Image Contrast in Topographs

3.1 Threading Dislocations

Threading dislocations are the most common *line defects* in crystals [37]. A threading dislocation is a one-dimensional structure consisting of imperfect ordering of atoms within the lattice, and it manifests itself as a one-dimensional chain of flawed packing of the atoms, continuing from atom to atom until it forms a loop or terminates at a crystal interface. The imperfect ordering of the atoms around a dislocation cannot be easily resolved, because practically all of the atoms around the dislocation core would need to be relocated simultaneously, and the energetic cost for that to happen is almost always too high. If only some portion of the atoms around the dislocation core would be moved to their correct lattice sites, the relocated atoms would simply force some of their neighboring atoms out of the lattice sites due to geometrical and preferred interatomic bonding length reasons, which would result in dislocation movement instead of dislocation annihilation. Because of their persistence, the threading dislocations have some properties that are similar to solid objects, namely they can move around and bend within the crystal lattice, and they cannot disappear or change without dislocation recombination or annihilation [38]. The dislocation movement is made possible by *dislocation gliding* [39], a process where the atoms change places a few at a time, and as a result the dislocation can move but not annihilate. As the threading dislocations are merely defects in the normal order of the lattice, they cannot exist without the lattice, and they necessarily either have endpoints on the crystal surface or form closed loops. The number of dislocations in a lattice can increase by *dislocation multiplication* caused by dislocation sourcing. One of the earliest discovered dislocation sourcing mechanism was the generation of the Frank-Read dislocation loops emerging from the Frank-Read sources [38, 39, 40, 41, 42].

3.2 Burgers Vector

Burgers vector $\vec{b}$ is used to describe the magnitude and direction of the lattice distortion caused by a dislocation [43]. Whenever there is a dislocation in the lattice, the lattice becomes distorted, and any closed lattice unit vector path around

the dislocation core has a discontinuity $\vec{b}$, which is the Burgers vector. Burgers vector $\vec{b}$ is a measure for the discontinuity of the lattice at the immediate environment of the dislocations, and the magnitude of the Burgers vector is measured in lattice units along a path around the dislocation core the Burgers vector belongs to. Figures 3.1 and 3.2 show illustrations of different dislocations having Burgers vector magnitudes of one lattice unit each, but the discontinuities (i.e. Burgers vectors $\vec{b}$) point into different directions compared to the dislocation line direction $\vec{\ell}$ in each of the lattices. The magnitude and direction of the Burgers vector stays constant along the dislocation line due to the same energetic and geometric reasons that prevent spontaneous dislocation annihilation without excess energy. The Burgers vector is also constant during dislocation gliding, and generally only changes when two or more dislocations combine. The dislocations in crystals are usually labeled after their Burgers vector and *slip plane*, which is a plane along which the dislocations can easily glide. The slip planes are usually the lattice planes with the highest atom packing density, and in the diamond and zincblende lattices they are the {111} planes. A dislocation with *slip distance* $a/\sqrt{2}$, Burgers vector $\vec{b} = a/2[110]$, and {111} slip planes would be written as $a/2\langle110\rangle\{111\}$. Such dislocations labeled as $a/2\langle110\rangle\{111\}$ were found in Publications I, II, IV, V, VII, and IX.

3.3 Edge Dislocations

A pure *edge dislocation* has its Burgers vector $\vec{b}$ exactly perpendicular to the dislocation line $\vec{\ell}$. Figure 3.1 shows a schematic representation of an edge dislocation with Burgers vector length $|\vec{b}|$ of 1 lattice unit. When a lattice has an edge dislocation, there is an extraneous half-plane of atoms within the lattice, and this superfluous half-plane terminates at the half-plane edge, which is the dislocation core. The shaded row of the lattice unit cells in Fig. 3.1 indicates the extraneous half-plane, which in a full lattice would continue indefinitely to the left, away from the dislocation core. Pure edge dislocations of type $a/2\langle110\rangle\{111\}$ were found in InAs in Publication I.
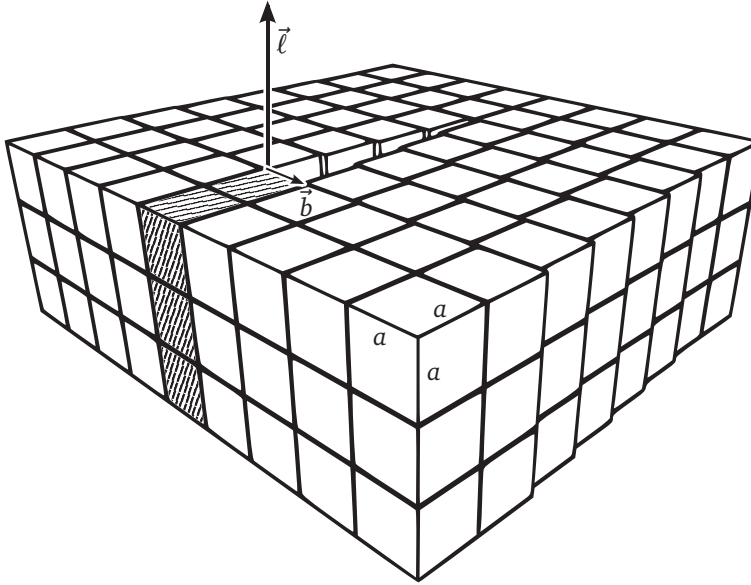
Figure 3.1: An illustration of an edge dislocation in a lattice of equal-sized cubes, where the Burgers vector length $|\vec{b}|$ equals the edge length a of the cubes. The cubes in the figure could represent the unit cells of a real cubic crystal. The extraneous half-plane of unit cells is indicated by shading, and the dislocation line direction by vector $\vec{\ell}$.

3.4 Screw Dislocations

A pure *screw dislocation* resembles a screw or a spiral staircase running about the dislocation core line at the center [39]. The Burgers vector $\vec{b}$ of the screw dislocation is parallel with the dislocation line. Figure 3.2 shows a schematic representation of a screw dislocation with Burgers vector length of 1 lattice unit. If the Burgers vector magnitude $|\vec{b}|$ of a screw dislocation is very large, there may form a small line-like void around the dislocation core. These void cores are usually called *micropipes* or *nanopipes*, and they are often found in hexagonal crystals, like the wurtzite GaN or wurtzite SiC [44, 45]. No micropipes were detected in the GaN samples of Publication VI, but regular pure screw dislocations of type $a/2\langle 110\rangle\{111\}$ were found in InAs in Publication VII.
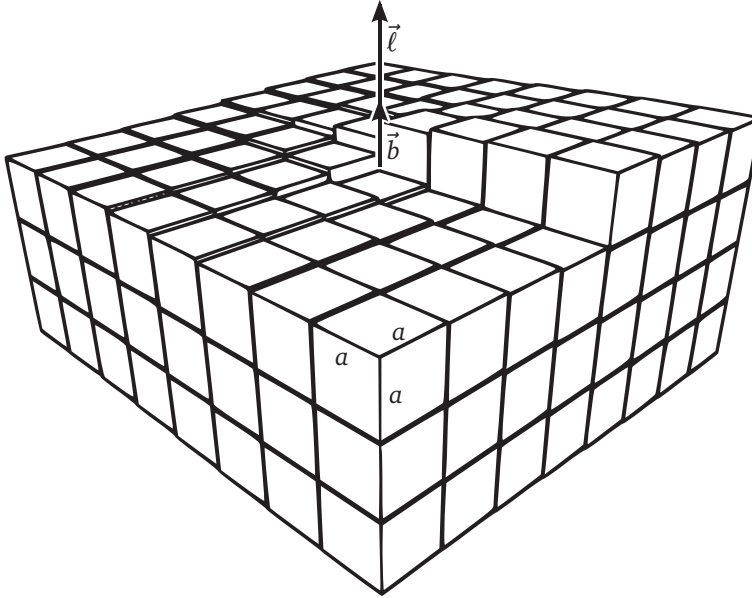
Figure 3.2: An illustration of a screw dislocation in a lattice of equal-sized cubes, where the Burgers vector length $|\vec{b}|$ equals the edge length a of the cubes. The cubes in the figure could represent the unit cells of a real cubic crystal. The dislocation line direction is indicated by vector $\vec{\ell}$.

3.5 Mixed Dislocations

Mixed dislocations are dislocations that contain both the edge and screw components. Most threading dislocations in real crystals follow a curved path and are therefore mixed. A dislocation following a curved path may actually change its type, because the dislocation line direction $\vec{\ell}$ changes along the path, but the Burgers vector $\vec{b}$ must stay constant. If at some point at the mixed dislocation arc $\vec{\ell}$ and $\vec{b}$ happen to be perpendicular, i.e. $\vec{b} \cdot \vec{\ell} = 0$, that small part of the dislocation is actually pure edge type. If the dislocation line is curved enough, there may also exist some other point or points at the dislocation arc where $\vec{\ell}$ and $\vec{b}$ are parallel, i.e. $|\vec{b} \times \vec{\ell}| = 0$, implying pure screw type at those points. However, between these points the dislocation arc must be of the mixed type. Perhaps the most common dislocation type in the diamond and zincblende lattices is the 60°⟨110⟩{111} mixed dislocation [46]. Mixed 60°⟨110⟩{111} dislocations were

observed in Publications II, IV, V and IX.

3.6   Extinction contrast

Dislocations produce image contrast in the X-ray topographs because the strain fields around the dislocation cores distort the lattice, which causes perturbations in the diffraction near the dislocation cores. The actual discontinuity at the dislocation core is very small, typically only a few ångströms wide. Because of the small size of the dislocation core itself, it does not produce any detectable contrast in the topographs. The visible dislocation images are actually the images of the strain fields formed around the dislocation cores in the crystal lattice. This kind of dislocation image contrast is called *the extinction contrast*, and it can be further subdivided into *the direct image contrast*, *the dynamical contrast* and *the intermediate contrast* [47].

3.6.1   Direct image contrast

If dislocation strain fields produce *extinction contrast* in low-absorption conditions, then the resulting topographs are called *direct images* with *direct image contrast*, which is also called *diffraction contrast*. [47]. When a polychromatic synchrotron X-ray beam travels through the lattice of a sample crystal, only one wavelength of X-rays is diffracted for given Miller indices *hkl*, because only that wavelength fulfills the Bragg condition for the indices *hkl*. The X-rays having the correct Bragg wavelength diffract multiple times inside the crystal, where their energy is distributed within *the Borrmann triangle*, which reduces the observed intensity on the topographs, because the original X-ray intensity on an incident beam path is spread onto multiple paths before the X-rays finally exit the Borrmann triangle and the crystal. Most of the X-ray wavelengths are not diffracted and thus go through the crystal in a single path without being diffracted. However, in real crystals where dislocations and other defects are practically always present, the strain fields around the dislocation cores bend the lattice locally, which slightly alters the angles of the Bragg condition just around the dislocation core. The small difference in the Bragg condition is enough to cause a close but distinct wavelength to be diffracted, instead of the characteristic wavelength diffracted in the undisturbed parts of the crystal lattice. But because the X-ray wavelength diffracted from the dislocation strain field is generally not diffracted

in the main volume of the crystal, the X-rays diffracted from the dislocation-bend lattice follow practically a single path through the crystal, and therefore exit the crystal as a more intense beam than the normally diffracted X-rays that are spread over the Borrmann triangle. Thus, in direct images the dislocations always produce more contrast than the near-perfect lattice around them [48]. In practice, the direct image synchrotron X-ray topographs have dark gray or black defect images on a lighter gray background.

Whether a particular experiment happens under low or high absorption conditions can be determined by the quantity $\mu_0 t$, which is the product of the average linear attenuation coefficient μ_0 and crystal thickness t, and is therefore the negated natural logarithm of the total attenuation $\exp(-\mu_0 t)$. For direct images, i.e. low attenuation, $\mu_0 t$ is necessarily quite small, because too heavy absorption would lead to impractically long exposure times. Generally, limit $\mu_0 t < 1$ is often given for direct images [47], but this should only be employed as a guidance, because the practical limit varies with measurement geometry, diffraction conditions, and even between superficially similar samples. Direct images, among another contrast types, were still observed for $\mu_0 t = 2.8$ in $\bar{1}\bar{5}1$ and $1\bar{5}1$ large-area transmission topographs of Publication I, which is likely caused by the reduction of the Borrmann effect for odd-ordered reflections in the zincblende lattice. Indeed, a more accurate analysis by A.R. Lang shows that the X-ray attenuation in crystals depends on the ratio of the imaginary parts of the structure factors $\varepsilon_0 = \mathcal{F}''_g / \mathcal{F}''_0$, so that the total attenuation depends strictly speaking on the quantity $\varepsilon_0 \mu_0 t$ rather than only on $\mu_0 t$ [49]. ε_0 is close to unity for even-ordered reflections in diamond or zincblende lattice, but is reduced for the odd-ordered reflections [49], which decreases the absorption and may cause direct image contrast.

The dislocation images can sometimes disappear in some topographs of the X-ray film, while still being visible on the others. This is caused by *the dislocation contrast disappearance*, which depends on the diffraction vector $\vec{g}$, the Burgers vector $\vec{b}$ and the dislocation line direction $\vec{\ell}$. The disappearance conditions are different for different dislocation types, so that the screw dislocation images disappear if $\vec{g} \cdot \vec{b} = 0$, but the edge dislocation images only disappear if both $\vec{g} \cdot \vec{b} = 0$ and $\vec{g} \cdot (\vec{b} \times \vec{\ell}) = 0$ [13, p. 199] [50]. Mixed dislocations by definition always have both the screw and edge components, and subsequently the contrast disappearance criterions for the mixed dislocations are the same as for the edge dislocations. *The partial contrast disappearance* for edge and mixed dislocations may occur, if $\vec{g} \cdot \vec{b} = 0$ and $\vec{g} \cdot (\vec{b} \times \vec{\ell}) \neq 0$, in which case the topograph would show only a faint contrast for the dislocations [13].

3.6.2 Dynamical contrast

The dynamical theory of diffraction takes the intensity exchange within the crystal fully into account [51]. These *dynamical diffraction* effects are based on interference and absorption inside the crystal between two incoming and two diffracted wavefields. The images of dislocations and other defects in *dynamical contrast* topographs may be both lighter or darker than background, and various interference effects are possible. However, dynamical contrast can only be observed in near-perfect crystals, because lattice defects tend to destroy the interference patterns, which results in extinction contrast. Dynamical X-ray diffraction images of dislocations in nearly perfect crystals are often light gray or white lines on dark background, because the local disturbance of the X-ray wavefront by the dislocation strain field destroys the exact Bragg condition of the wavefield near the dislocation core, which prevents the wavefield from forward-diffracting, and it will be absorbed instead. Because of this diffraction-shadowing effect the dynamical images were originally called *extinction shadows* [52].

Transmission section topography performed on near-perfect crystals often yields *Pendellösung fringes* on the topograph. Pendellösung fringes are contrast fringes where lighter and darker contrast stripes alternate on the topograph. The fringes are caused by interference effects of the diffracted wavefronts, and the phenomenon can be fully modeled with the dynamical theory of diffraction. Efficient calculation models for computer simulation of the Pendellösung fringes and other dynamical contrast effects have been developed in the past [53, 54]. Pendellösung fringes are often found in topographs of Si wafers due to the generally excellent quality of modern Si substrates, which is the case in one of the transmission section topographs of Si substrates in Publication III, where Pendellösung fringes can be seen clearly. The 311 transmission section topograph of an InP ELO layer on Si sample from Publication III is reproduced in Fig. 2.11.

If absorption of the crystal is too strong in transmission topography geometry, there will be no observable direct contrast in the X-ray detector, because the crystal itself absorbs all the diffracted X-ray energy. As the observed contrast depends on detector sensitivity, exposure time, and X-ray beam energy, there is no exact limit for complete attenuation, but $\mu_0 t > 6$ has been considered as a practical limit of attenuation for extinction contrast [48, 47]. However, exceeding the practical limit for $\mu_0 t$ does not necessarily mean that topographs cannot be recorded in transmission geometry. In case the sample is a near-perfect single crystal, the X-rays may undergo *anomalous transmission*, which is also called *the*

Borrmann effect [51]. If anomalous transmission, which can be modeled by the dynamical theory of diffraction, occurs in the sample crystal, *dynamical image contrast* can be produced even if the absorption is so large that no contrast would normally be expected [51]. Anomalous transmission is caused by the interference of the two incident and the two diffracted wavefields, where the wavefield having its antinodes at lattice sites is greatly attenuated, but the other wavefield having its nodes at lattice planes undergoes only a slight attenuation [51]. Consequently, the contrast in anomalous transmission topographs is dynamical, i.e. the defect images have lighter contrast against the darker background of the perfect lattice.

3.6.3 Intermediate Contrast

If absorption is close to the limit between extinction contrast and dynamical contrast (i.e. $1 < \mu_0 t < 6$), it is possible that the topographs show *intermediate contrast*, where parts of the image are formed by kinematical contrast and other parts by dynamical contrast. Some of the defect images in such topographs are lighter and some darker than the background. Dislocation contrast disappearance criterions for dynamical contrast (and thus for intermediate contrast) are the same as they are for the extinction case, i.e. dynamical images of screw dislocations disappear if $\vec{g} \cdot \vec{b} = 0$, and dynamical images of edge dislocations disappear if both $\vec{g} \cdot \vec{b} = 0$ and $\vec{g} \cdot (\vec{b} \times \vec{\ell}) = 0$ [13, p. 199].

3.7 Orientation Contrast

Contrast in topographs can also be caused by variations in lattice orientation. Spatially different parts of the lattice may have different orientations, either by macroscopic bending of the crystal or through grain boundaries. Also, in the case of thin films of heterostructure semiconductors, the epitaxial layer may grow tilted due to lattice mismatch $f = \Delta a / a = (a_f - a_s)/a_s$ caused by the difference between the epitaxial thin film lattice constant a_f and the substrate lattice constant a_s [55]. Such tilted epitaxial layers were observed in GaAs on Ge heterostructures (Publications II and IV), in GaN on sapphire heterostructures (Publication VI), and in GaInP on GaAs buffer layer on Ge (Publication IX).

If two or more areas of the crystal have different orientations, the respective diffracting crystal planes of the areas are also at an angle, and thus diffract distinct wavelengths to distinct directions, which results in *rotational orientation contrast*. Rotational orientation contrast usually produces both darker and lighter areas on the film, because the total diffracted intensity is not altered much, but the distribution of the intensity on the topograph changes. Generally, the image of the part of the crystal having the different lattice orientation is displaced on the topograph in respect to the image of the main crystal volume. Depending on the direction of the angular difference, the displaced image partially overlaps the image of the main crystal, which leads to dark contrast on the overlapping area. On the other hand, on the opposite side of the displaced image there is an area that receives no intensity from the main crystal volume nor the differently oriented part of the crystal, which results in lighter contrast on that area.

Rotational orientation contrast does not depend on the Miller indices *hkl* of the diffraction in any way. However, *strain-induced orientational contrast*, which is caused by lattice deformation by strain, is only observed in cases where the diffraction vector $\vec{g}$ is not parallel nor perpendicular to the relevant strain component [55]. Figure 3.3 shows schematic representations of effects of strain and orientation changes to X-ray angles. Distinct contrast changes possibly visible in topographs include Figure 3.3 a) strain-induced asymmetric, b) strain-induced symmetric, c) rotational asymmetric, and d) rotational symmetric. By comparing several topographs with different Miller indices on the same X-ray film, it is generally possible to deduce whether the contrast changes are caused by strain, orientation changes, or their combination. Such comparison has been done in Publication III for lateral epitaxially overgrown InP structures on Si.

The SR-XRT has proven to be an able tool for studying the strain, crystal quality and lattice orientation of the epitaxial lateral overgrowth (ELO) layers [56]. In Publication III the InP ELO epitaxial stripes were shown to have both the rotational orientation contrast caused by the growth tilt, and also the strain-induced orientation contrast caused by the residual strain from the epitaxial process. The occurrence of both the rotational and strain-induced orientation contrasts together is to be expected in the highly strained epitaxial layers due to the growth tilt effect [55]. Indeed, similar occurrences were observed in the GaN thin films on sapphire of Publication VI, and the GaInP on GaAs buffer layers on Ge heterostructures of Publication IX, which both exhibited considerable strain. The orientation contrast of the X-ray topography, be it rotational or strain-induced, is fully visible in the white beam topography only, because the different lattice orientations diffract different X-ray wavelengths. In practice, the topography sys-
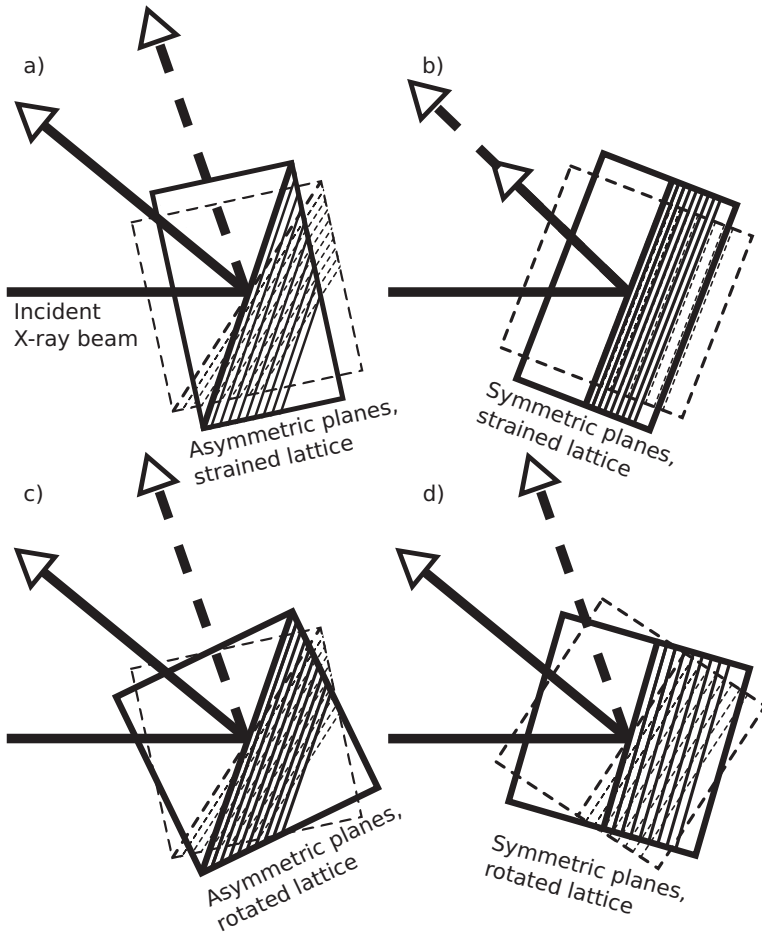
Figure 3.3: X-ray diffraction affected by orientation and strain. **a)** The lattice strain without the lattice rotation modifies the X-ray angles for the asymmetric diffraction, **b)** the lattice strain without the lattice rotation does not change the X-ray angles for the symmetric diffraction, **c)** the lattice rotation without the lattice strain modifies the X-ray angles for the asymmetric diffraction, and **d)** the lattice rotation without the lattice strain modifies the X-ray angles for the symmetric diffraction. The undisturbed lattice planes and the corresponding diffracted beams are drawn with dashed lines, whereas the strained and rotated lattice planes and the corresponding diffracted beams are drawn with solid lines. Wide enough X-ray spectrum of the source is assumed, so that diffractions may occur with different Bragg angles θ and wavelengths λ.

tems utilizing highly monochromatic characteristic X-ray radiation, such as Lang cameras, only show one of the different orientations at the time, even though there is usually only a minute difference in the wavelengths. On the other hand, SR-XRT is particularly well-suited for samples having strong orientational contrast due to the wide and uniform spectrum of the synchrotron radiation. However, under extreme lattice strain *double diffraction* may occur within the lattice, which produces additional white and black contrast lines onto the topograph [57], thus further complicating the interpretation of the topographs.

3.8   Stereo Pair Topographs

In the large-area geometries, it is possible to obtain *stereo pair topographs* by selecting two topographs from the same exposure and combining them into the same stereoscopic image. The two topographs must have reasonably similar attenuation lengths, and their diffraction vectors $\vec{g}$ should form a suitable projection geometry, because the attenuation lengths and the diffraction vectors directly determine the viewing depth and viewing angles of the stereo pair. The stereo pair topographs can be made both in the transmission and back-reflection geometries [58].

In practice, useful stereo pairs can be found by looking at every topograph on the film, and choosing a pair with adequately similar visual properties. From a well-selected stereo pair it is possible to deduce depth information about the defects, such as the three-dimensional paths of the dislocations. The stereo pair topographs are particularly useful for imaging epitaxial multilayer samples, where the depth information can be exploited in order to find out how the dislocations interact with the layer interfaces. Figure 3.4 shows a stereo pair of the $\bar{1}5\bar{1}$ and $1\bar{5}1$ large-area transmission topographs of an InAs sample of Publication I. By crossing one's eyes and focusing each eye to the picture on the opposite side of the eye, it is possible to see the dislocation images stereoscopically without any extra instruments.
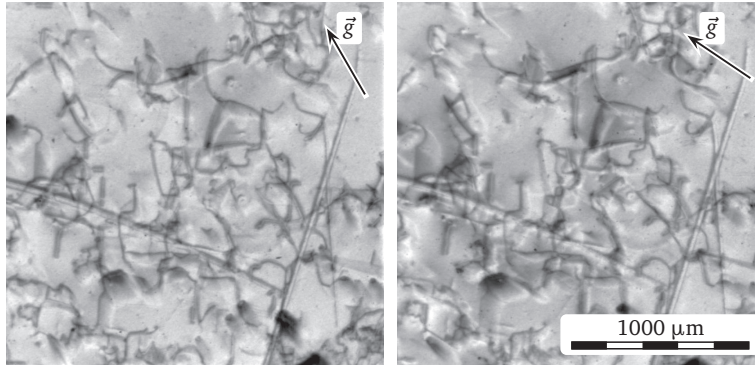
Figure 3.4: Stereo pair of $\bar{1}5\bar{1}$ (left) and $1\bar{5}1$ (right) large-area transmission topographs of an InAs sample of Publication I. The features in the topograph are images of threading dislocations, the density of which is $\approx 2 \times 10^3$ cm^{-2}. Diffraction vector $\vec{g}$ projections are indicated.

3.9 Precipitate and Void Image Contrast

In addition to the dislocations, also other defects cause strain in the crystals. In some cases, the strain fields caused by the precipitates and voids in the crystal may cause visible contrast in the topographs. Generally, the strain fields caused by the point defects are more spherically symmetric the farther away from the point defect the strain fields are observed. Because the precipitates and voids are usually very small, their strain fields can be approximated to be spherically symmetric. The core strain is tensile in the voids, but the precipitates most often have compressive strain in their cores, although tensile strain for the precipitate cores is also possible. The contrast in the topographs depends on the type of the strain, which makes it often possible to deduce whether a given strain field contrast in the topograph is caused by a precipitate or a void.

A spherically symmetric strain field of a crystal defect causes dynamical topograph image contrast consistÃ◯ng of two half-discs, one of which is dark and the other light [48]. If the strain field is compressive in the core, i.e. in the case of a precipitate, the dark half-disc is on the positive side and the light half-disc on the negative side of the diffraction vector $\vec{g}$ projection [48]. Consequently, if the strain field is tensile, the light half-disc is on the positive and the dark half-disc on the negative side. Enlargements of the large area transmission topographs show-
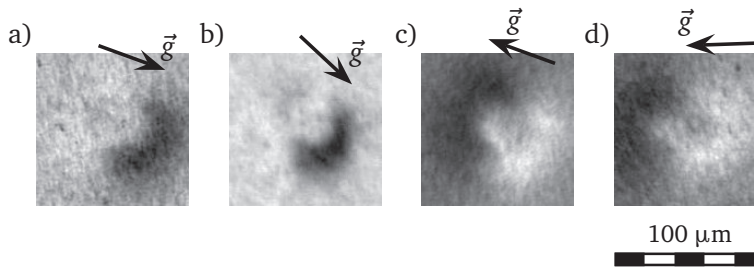
Figure 3.5: Enlargements of **a)** $\bar{5}\bar{1}1$, **b)** $\bar{5}11$, **c)** 511, and **d)** 531 large area topographs showing the same precipitate in a thin 210 nm GaAs film on Ge substrate. The contrast pattern of the precipitate follows the indicated diffraction vector $\vec{g}$ projection.

ing such contrast differences were analyzed in Publication IV. Figures 3.5 a)–d) are reprinted from the publication, and the images are indicative of the radially symmetric precipitate strain field with mainly compressive strain around its core, although the strain very close to the core appears to be very small and possibly even tensile, as evidenced by the faint opposite color half-disks in the center of the main precipitate image.

3.10 Grain Boundary Image Contrast

Polycrystalline matter consisting of *grains*, i.e. individual crystallites, can be studied by the SR-XRT provided that the grains are sufficiently large. Generally, if the individual grains are larger than about 10 μm they may be resolvable in the high-resolution synchrotron topographs, which have the maximum practical spatial resolution of about 1 μm [25]. In any case, the larger grains offer more information about the crystals, because the internal strain within the small grains is usually so high that the contrast produced by the other defects present is overshadowed by the grain boundary contrast. The polycrystal grains having large-angle grain boundaries generally show clear orientation contrast, so that the grain images in the topographs fragmentate to a set of distinct images, the spacing between which depends on the grain angles and the exposure geometry. For some grain angles and topography geometries the grain images can be overlapped, in which case it may be difficult to determine the grain that has caused a given feature on the film.

Inbetween the true single crystals and the polycrystalline matter there exists a class of materials that are not exactly neither, but have properties of both. The *small-angle granular* crystals consist of *the small-angle grains* bordered by the dislocation chain boundaries, so that the lattice of the individual crystallites are almost in the same lattice, but not exactly [59, 60]. The dislocations forming the small-angle grain boundaries may or may not resolve to individual dislocations in the synchrotron X-ray topographs, depending on the inter-dislocation distances, and thus on the grain boundary angles. The InP ELO layers of Publication III have small-angle crystal boundaries with maximum tilt angle of 0.06° between the crystallites, and they must therefore be considered as small-angle granular crystals, which can be classified either as mono- or polycrystals depending on the classification criteria.

4 Thin Epitaxial Films

Semiconductor devices are most often built on polished monocrystal substrate surfaces, i.e. *crystal wafers*. There are two main strategies used for producing the semiconductor devices on the crystal wafers, the first is the diffusion or implantation of the dopant atoms of different elements into the substrate, and the second is *the epitaxy* of thin film device layers on the substrate. In contrast to the implantation methods, the epitaxial growth of the thin films does not damage the substrate crystal. However, if the epitaxial film is too thick, the differences in the lattice constants and the thermal expansion coefficients between the substrate and the epitaxial film may result in formation of crystal defects caused by the strain. Thus, most of the epitaxial films used in the semiconductor devices are relatively thin.

The epitaxy processes are based on the deposition of new atoms on the lattice sites on top of the previously grown atom layers. The liquid phase epitaxy (LPE) process was the first viable epitaxy method used in the semiconductor industry. In addition to the LPE, the vapor phase epitaxy (VPE) methods, such as the metal-organic vapor phase epitaxy (MOVPE) and the hydride vapor phase epitaxy (HVPE), the molecular beam epitaxy (MBE), and the solid phase epitaxy (SPE) are all used in the modern semiconductor processes. Even though the different growth processes differ significantly in their source material delivery and other details, the growth methods themselves do not primarily define the lattice strain, which rather depends on the differences in the lattice constants and thermal expansion. Thus, when determining the maximum theoretical thickness of a thin epitaxial film on a thick crystal substrate, the exact type of the epitaxial method often does not need to be taken into account.

4.1 Misfit Dislocations

In principle, the experimental determination of the thin film critical thickness should be done by the direct observation of the formation of *the misfit dislocations* (MD). However, most of the *in situ* measurement apparatuses are ill-suited for detecting a small number of MDs on the epitaxial film. As a result, the relaxation of the epitaxial thin film may be experimentally observed much later than immediately after exceeding the critical thickness. Direct *ex situ* observation of

the individual MDs is possible with SR-XRT. The misfit dislocations in the thin epitaxial films reduce the epitaxial stress of the film. Each new MD relaxes the stress, but only by a very small amount when compared to the total stress in the layer. If the epitaxial process is continued beyond the critical thickness, the increased stress rapidly produces a great number of MDs. These MDs generally form *a misfit dislocation network*, where the MDs are aligned on the crystallographically preferred orientations. If epitaxial growth is performed on the {100} planes of the diamond or zincblende crystals, the preferred MD line directions $\vec{\ell}$ lie along the ⟨110⟩ directions on the epitaxial surface.

The misfit dislocations can be of the edge, screw or, mixed types, depending on the crystal lattice, the surface orientation of the epitaxial plane, and the type of the epitaxial structure. Perhaps the most common type of MDs in group IV diamond and group III-V zincblende lattice semiconductors are the 60°⟨110⟩{111} mixed dislocations [61, 62, 46], which have a 60° angle between their dislocation lines $\vec{\ell}$ and Burgers vectors $\vec{b}$, although the pure edge dislocations are also possible [63]. MDs in the homoepitaxy of the strongly doped epitaxial layers were observed in Publications I, VII and VIII. In the heteroepitaxy, where MDs are more common, MD networks were found and characterized in Publications II, IV, V, and IX, of which Publication V discussed MDs in *the dilute heteroepitaxy*. Most of the observed MDs were mixed 60°⟨110⟩{111} dislocations, but in Publication I pure edge MDs in InAs were found, and in Publication VII somewhat rare interfacial pure screw MDs in GaAs were found.

4.2   Critical Thickness

It is almost always desirable, that the epitaxial growth of atom layers on single crystal substrates will result in the new atoms to be positioned in the lattice sites of the original crystal lattice. This is generally true in the homoepitaxy as well as in the heteroepitaxy, for which there is a possibility of distinct lattice constants of the epitaxial layer and the substrate crystal. If the lattice constants of the layers do not differ too greatly, the epitaxial layer atoms may still occupy the correct lattice sites of the substrate crystal, but an extra amount of strain energy builds up for every atom that is not in the equilibrium distance of its neighbors. The epitaxial layer strain may be either compressive or tensile along the relevant crystal axes within the layer surface. Because all of the known group IV and III-V semiconductor crystals have Poisson's ratio v greater than 0 but less than 0.5 [11], the strain in the epitaxial layer surface normal direction has the opposite

sign to the strain in the epitaxial layer surface directions.

For the semiconductor alloys consisting of a combination of three or more distinct elements, e.g. $Ga_{1-x}In_xP$, the lattice constant of the ternary alloy can be approximated by *Vegard's law* [64]

$$a(A_{1-x}B_xC) = (1-x)a(AC) + xa(BC), \qquad (4.1)$$

which is the linear combination of the lattice constants a of the constituent binary alloys AC and BC weighted by their relative proportion in the alloy.

The buildup of the epitaxial layer stress is governed by the lattice constant difference and the layer thickness. Eventually, if the epitaxial layer is grown thick enough, the stress energy grows large enough for the stress-induced crystal defects to appear. The thickness at which the stress begins to relax by the defects is called *the critical thickness* of the thin film. In addition to the epitaxial layer thickness and the lattice constant differences, the critical thickness also depends on the temperature differences and overall mechanical qualities of the thin film. Moreover, any external strain may play a significant role in practical situations. Notwithstanding the external strain and the mechanical quality issues, it is possible to derive equations for the stress buildup as a function of the epitaxial layer thickness, and compare the value to the formation energy for the formation of the known strain-relaxing dislocation types. This was first done by Matthews, Mader and Light who showed that by utilizing the mechanical equilibrium theory for minimizing the total energy of the strained epitaxial layer structure and assuming a periodic array of MDs having a known dislocation energy, it is possible to predict the critical layer thickness h_c for a given MD type [65]. Matthews and Blakeslee enhanced and further established the validity of the Matthews-Blakeslee model in a series of articles [66, 67, 68] in Journal of Crystal Growth. Over the years, the mechanical equilibrium theory for calculating the critical thicknesses h_c of the thin films has been generally found to reasonably agree with the experimental results [69], even though there have been various hypotheses about the dislocation energies and other terms in the equations involved [65, 66, 67, 70, 71, 72, 73, 74]. The equations for the critical thickness h_c derived from the equilibrium theory are generally of the form

$$h_c \approx \frac{|\vec{b}|}{\Omega|f|} \left[\frac{1 - \nu \cos^2 \alpha_b}{(1+\nu)\cos \lambda_b} \right] \left[\ln \left(\frac{h_c}{b} \right) + \Gamma \right], \qquad (4.2)$$

in which ν is the substrate Poisson ratio, $f = \Delta a/a$ is the lattice mismatch, $|\vec{b}|$ is the slip distance for the MDs i.e. the Burgers vector magnitude, $\alpha_b = \measuredangle(\vec{u}, \vec{b})$ is

the angle between the MD line direction $\vec{u}$ and the MD Burgers vector $\vec{b}$, and the angle $\lambda_b = \measuredangle(\vec{b}, \vec{u} \times \vec{n})$, where $\vec{n}$ is the sample surface normal [65]. The Poisson ratios of III-V semiconductors are reasonably close to $\nu \approx 0.333$ [11], and the misfit relaxation normally happens by $60°$ $\frac{a}{2}\langle 101\rangle\{111\}$ MDs, which corresponds to values $|\vec{b}| = a/\sqrt{2}$ and $\cos\alpha_b = \cos\lambda_b = \frac{1}{2}$. Ω and Γ are parameters related to the tension inflicted by the MD lines, and they differ between authors. In [70] Matthews assumed pure edge dislocations and used $\Omega = 8\pi$ and $\Gamma = 1$. For the more general case Matthews, Mader and Light give values $\Omega = 8\pi$ and $\Gamma = 0$ in [65] for single epitaxial layers, which is interestingly the same as used by Fischer, Kühne and Richter using another approach for the equilibrium theory [71]. However, Fischer *et al.* derived an extra term

$$\frac{|\vec{b}|\cos\lambda_b}{2|f|} \tag{4.3}$$

directly added to the right side of equation (4.2) [71]. Based on the different assumptions about the dislocation energies, Houghton derives $\Omega = 8\pi$, but $\Gamma = \ln(4) \approx 1.39$ [73]. Paul suggests $\Omega = 2\pi$ and $\Gamma = 1$ [75], which are also the values given by Matthews and Blakeslee for multilayer structures [66, 67]. Calculations made by Rockett yield $\Omega = 4\pi$, when taking into account various dislocation interactions [74]. Generally, values $\Omega = 2\pi$, 4π and 8π can be found in the literature, and Ω is the parameter giving the largest effect on the critical thickness calculation.

Regardless of the model used for the calculation of the thin film critical thicknesses, the effects of the temperature variations must be taken into account due to the relatively high growth temperatures of the single crystal thin films. The lattice mismatch f in heterostructures depends on the temperature because the linear thermal expansion coefficients α_{ltc} is usually different for different semiconductor crystals. It is thus necessary to consider the critical thickness h_c for the largest strain f within the temperature ranging from room temperature to the heterostructure growth temperature. Due to the thermal strain there often is a perfect lattice match for the heterostructures only at a specific temperature. Over a larger temperature range, there is rather a maximum of the attainable critical thickness h_c of heterostructures, as shown in Publication IX, where the experimental results for the samples A and B are compared to the calculated critical thicknesses. The samples studied in Publication IX consisted of GaInP thin films grown at 610 °C on GaAs buffer layer on Ge substrates. The sample properties are listed in Table 4.1, and it should be noted that only sample B contained misfit dislocations. The experimental data demand that for an accurate critical thickness model sample A should lie slightly below the realistically simulated h_c

Table 4.1: Properties of samples A and B of Publication IX. $Ga_{1-x}In_xP$ lattice mismatches to Ge $f = \Delta a/a = (a_{Ge} - a_0)/a_0$ (a_0 is the stress-free bulk lattice parameter of the $Ga_{1-x}In_xP$ epitaxial layer) at room temperature (RT) are calculated from the measured lattice spacings, whereas at 610°C they have been extrapolated using RT linear thermal expansion coefficients α_{ltc} from [76, 77] and lattice constants from [78, 79, 80].

	sample A	sample B
GaAs buffer thickness (μm)	0.23	0.24
$Ga_{1-x}In_xP$ thickness h (μm)	1.0	1.0
$Ga_{1-x}In_xP$ In content x	0.5005	0.4906
$f = \Delta a/a_0$ for $Ga_{1-x}In_xP$		
at RT	-3.5×10^{-4}	$+3.8 \times 10^{-4}$
at 610 °C	$+3.6 \times 10^{-4}$	$+10.9 \times 10^{-4}$
Calculated h_c for $Ga_{1-x}In_xP$ (μm)		
at RT	2.43	2.22
at 610 °C	2.36	0.68

curve, provided that the simulated curve would take into account the temperature difference between the growth temperature at 610 °C and room temperature. Choosing $\Omega = 2\pi$, $\Gamma = 1$ and utilizing the lattice mismatches $f = \Delta a/a$ from Table 4.1 at RT, equation (4.2) gives the critical thicknesses of $h_c \approx 2.43$ μm for sample A and $h_c \approx 2.22$ μm for sample B, which are both well above the actual 1 μm $Ga_{1-x}In_xP$ epitaxial layer thicknesses. However, using the lattice mismatches f at the growth temperature 610 °C from Table 4.1, the critical thickness for sample A ($h_c \approx 2.36$ μm) is still much larger than the actual epitaxial layer thickness, but the critical thickness of sample B reduces to $h_c \approx 0.68$ μm, which is less than the actual $Ga_{1-x}In_xP$ layer thickness of 1 μm. Thus, the results of the Matthews-Blakeslee model with $\Omega = 2\pi$ and $\Gamma = 1$ agree rather well with the observed MD structure on the samples, provided that the effect of the growth temperature and the distinct linear thermal expansion coefficients α_{ltc} are taken into account. The critical thickness curves with the thermal effects of cooling down from the growth temperature to RT are plotted in Fig. 4.1.

As pointed out, sample A is below the h_c curve in Fig. 4.1 only for the values $\Omega = 2\pi$ and $\Gamma = 1$ in equation (4.2) as suggested by Paul for the single epitaxial layers [75] and Matthews and Blakeslee for the multilayer structures [66, 67]. This is interesting, because according to [66] $\Omega = 2\pi$ should only be valid for the repeating multilayer structures, and Paul in [75] does not substantiate in detail the reason for selecting $\Omega = 2\pi$. One possible explanation for the larger
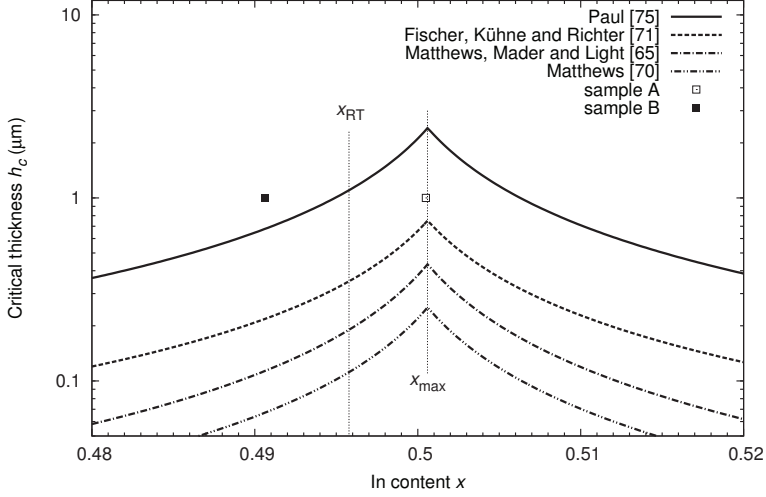
Figure 4.1: Simulated critical thicknesses of the $Ga_{1-x}In_xP$ on Ge structure of Publication IX. The critical thicknesses are plotted as a function of In content x, as calculated by combining simple linear thermal expansion and the theoretical models for critical thickness suggested by Paul [75], Fischer *et al.* [71], Matthews *et al.* [65], and Matthews (assuming relaxation through pure edge dislocations) [70]. Vertical dotted lines indicate In contents x_{RT} of the $Ga_{1-x}In_xP$ lattice matched to Ge at room temperature and x_{max} of the maximum attainable critical thickness within the full temperature range. Only sample B actually contains misfit dislocations.

than expected critical thickness observed in sample A could be the epitaxial layer growth tilt releasing some of the strain due to geometrical reasons [55]. Another explanation could be the lack of the threading dislocations in Ge substrates and GaAs buffer layers, because the threading dislocations normally act as the sources for the MD formation in the Matthews-Blakeslee model. However, in the GaInP/GaAs/Ge structures it is likely that the hillocks in the GaInP layer could act as the MD sources, but they may also restrict the free movement of the MD ends. In the original Matthews-Blakeslee model the both sides of the MD elongate, as the threading dislocations in the both ends of the MD can glide [70]. Regardless of the parameter Ω in equation (4.2), the Matthews-Blakeslee model appears to explain rather well the fact that there are MDs in sample B but not in sample A, provided that the linear thermal expansion coefficients α_{ltc} are taken into account.

5 Defects in Heterostructures

5.1 Doped Interfaces

Structures consisting of undoped and highly doped layers are considered homostructures, but they may exhibit characteristics that are similar to heterostructures due to the lattice mismatch caused by the dopant atoms. Publication I discusses defects in InAs n-i structures, where the n-layers were highly doped InAs and the intrinsic i-layer was undoped InAs. A misfit dislocation network was detected in one of the samples, where a 10 µm thick intrinsic epitaxial layer was grown on a relatively highly doped InAs substrate. In addition to the MD network all the InAs samples had circular arc threading dislocations, the density of which was ≈ 2000 cm^{-2}. Publications VII and VIII discuss GaAs p-i-n structures intended to be used in X-ray detector applications. In these publications the occurrence of MDs in highly doped layered homostructures was again confirmed, and the detrimental effect of the MDs to the electrical properties of the components was demonstrated in publication VIII. Some of the MDs seen in the samples of Publication VII were relatively rare pure screw MDs of type $|\vec{b}|\langle 110\rangle\{111\}$ with unknown Burgers vector magnitude, and it was found that the MDs originated from the endpoints of the threading dislocations residing in the bulk of the sample.

5.2 Dilute Heterostructures

Dilute heterostructures are semiconductor crystals having an additional minute amounts of an additional species of element added to the base crystal. The fraction of the atoms of the diluting element is much larger than in conventional doping, but not enough to completely change the crystal structure of the original semiconductor material, which would warrant a completely new compound semiconductor. Typically, dilute heterostructures have a few percentage of the additional matter, so that e.g. GaAs$_{1-z}$N$_z$ may contain nitrogen up to 5 % (i.e. $z < 0.05$). In respect to lattice constant mismatches dilute heterostructures such as GaAsN on GaAs are an intermediate step between highly doped homostructures and true heterostructures. Defects of dilute GaAsN with $\approx 0.85\%$ N content grown on GaAs by MOVPE are studied in Publication V. Topographs recorded

from four samples show that the critical thickness of such structures is about 0.5 μm, after which the MD formation begins.

5.3   Two-layer Heterostructures

True heterostructures are semiconductor crystals consisting of layers, where the layers are made of distinct materials, but together form a single common crystal structure. The individual layers in such structures may be elemental semiconductors or compound semiconductors, and they may additionally have been doped or diluted. True heterostructures are often the most difficult form of epitaxy, because problems arise from lattice mismatch, thermal expansion, material diffusion, and formation of anti-phase domains (APD). Publications II, III, IV, VI & IX discuss defects in true heterostructures consisting of an epitaxial layer and a substrate. Growth procedures of GaAs on Ge heterostructures are discussed in Publication II, where growth of thin APD-free GaAs layers grown on commercial Ge substrates is demonstrated. The quality of the GaAs epitaxial layers is studied in Publication IV, which is a SR-XRT topography study of the MOVPE-grown GaAs layers and the Ge substrates, and the formation of MDs in GaAs layers grown over the critical thickness was seen as expected. A large lattice mismatch between Si and InP in the samples of Publication III causes significant problems in epitaxy, which was partly overcome by using epitaxial lateral overgrowth (ELO) technique. Small-angle grain boundaries and other defects of the ELO InP layers on the Si substrate were studied by means of SR-XRT, XRD, and HR-XRD, and it was found that the maximum grain boundary angle was about 0.06°. Similar very small-angle boundaries of crystallites were found in epitaxial GaN on sapphire samples imaged by SR-XRT in Publication VI. The crystallite boundary tilt angles where so small, that the GaN thin film could in fact be considered to be single crystalline. In addition to the GaN thin film results, a cellular network of highly strained boundaries of ≈ 30 μm cells was observed on the sapphire substrate. The strain-cells are inflicted to the substrate by the epitaxial GaN layer.

5.4   Multilayer Heterostructures

Multilayer heterostructures are heterostructures containing more than two layers of different compositions. GaInP thin film on GaAs buffer on Ge substrate multi-

layer heterostructures and their defects are discussed in publication IX, where SR-XRT, XRD, and HR-XRD were used to collect information about the heterostructure crystals. The GaAs buffer on Ge substrate part of this multilayer heterostructure is effectively discussed in publications II and IV, for which the GaInP on GaAs on Ge layer structure is the natural extension of. MD formation on the GaInP on GaAs on Ge structure was extensively studied. Thermal expansion effects were added to the Matthews-Blakeslee critical thickness model, which proved out to be essential for explaining the observed MD formation behavior. The most striking feature observed in the topographs of publication IX are the truncated InP pyramids on the GaInP layer. These truncated pyramids are spontaneously formed during the MOVPE growth process of the GaInP layer.

5.5   Pyramidical Epitaxial Hillocks

The formation of pyramidical epitaxial hillocks on GaInP thin films grown on GaAs have been known for some time [81, 82], and not surprisingly, similar hillocks were found on GaInP on GaAs buffer on Ge heterostructures of Publication IX. Because the hillocks have clearly defined rigorous shapes, and they are equidimensional and grown into the same orientation, it is rather straightforward to conclude that they are crystallites with relatively well-defined properties. Growth techniques avoiding the formation of the hillocks on GaInP have been developed based on phosphine modulation during growth [83], but they still pose a significant problem for more straightforward growth methods. Nevertheless, their exact crystal structure had not been previously discovered despite efforts [81, 84, 85, 86, 87], but the XRD measurements of Publication IX revealed that the pyramid hillocks are made of crystalline InP, and are each formed by at least ten distinct crystal grains grown together into a rigorously defined structure. GaInP layers on GaAs have another type of surface defects, the so-called *arrow defects*, which are arrow-shaped formations on the GaInP layer that are considerably flatter than the pyramid hillocks [87, 88]. These arrow defects were notably completely absent from the GaInP layers on GaAs buffers on Ge of Publication IX.

References

[1] J. D. DANA: Manual of mineralogy, Durrie & Peck, 7th ed. (1855).

[2] A. NUSSBAUM: The mystery of the fifteenth Bravais lattice, *Am. J. Phys.* **68** (2000) 950–954.

[3] D. SHECHTMAN, I. BLECH, D. GRATIAS and J. W. CAHN: Metallic Phase with Long-Range Orientational Order and No Translational Symmetry, *Phys. Rev. Lett.* **53** (1984) 1951–1953.

[4] W. C. RÖNTGEN: On a New Kind of Rays, *Nature* **53** (1896) 274–276.

[5] W. FRIEDRICH, P. KNIPPING and M. LAUE: Interferenzerscheinungen bei Röntgenstrahlen, *Annalen der Physik* **346** (1913) 971–988.

[6] M. LAUE: Eine quantitative Prüfung der Theorie für die Interferenzerscheinungen bei Röntgenstrahlen, *Annalen der Physik* **346** (1913) 989–1002.

[7] M. LAUE and F. TANK: Die Gestalt der Interferenzpunkte bei den Röntgenstrahlinterferenzen, *Annalen der Physik* **346** (1913) 1003–1011.

[8] W. H. BRAGG and W. BRAGG: The Reflection of X-rays by Crystals, *Proc. R. Soc. Lond. A* **88** (1913) 428–438.

[9] B. D. CULLITY: Elements of X-ray Diffraction, Addison-Wesley Series in Metallurgy and Materials, Addison-Wesley Publishing Company, Inc., 1st ed. (1956).

[10] B. E. WARREN: X-ray Diffraction, Addison-Wesley Series in Metallurgy and Materials, Addison-Wesley Publishing Company, 1st ed. (1969).

[11] O. MADELUNG (ed.): Semiconductors: Data Handbook, vol. III/17A–22A–41A1a, Springer-Verlag (2004), ISBN 3-540-40488-0.

[12] E. ILIOPOULOS, K. F. L. JR. and T. D. MOUSTAKAS: Complex ordering in ternary wurtzite nitride alloys, *J. Phys. Chem. Sol.* **64** (2003) 1525–1532.

[13] D. K. BOWEN and B. K. TANNER: High Resolution X-ray Diffractometry and Topography, Taylor & Francis Ltd. (1998).

[14] K. HORAN, A. LANKINEN, L. O'REILLY, N. S. BENNETT, P. J. MCNALLY, B. J. SEALY, N. E. B. COWERN and T. O. TUOMI: Structural and electrical characterisation of ion-implanted strained silicon, *Mat. Sci. Eng. B* **154–155** (2008) 118–121.

[15] T. O. Tuomi, C. Paulmann and A. Lankinen: Private communications based on measurements and HASYLAB Internal Report "Strahlrohrdokumentation Fächer F. 29.07.92".

[16] R. Gehrke, H. Graafsma, L. Incoccia-Hermes, W. Laasch, T. Laarmann, W. Morgenroth, R. Röhlsberger, R. Treusch, U. Vainio and M. von Zimmermann (eds.): Photon Science 2011, Deutsches Elektronen-Synchrotron DESY, Notkestr. 85, 22607 Hamburg, Germany (2011). HASYLAB Annual Report.

[17] T. Tuomi, K. Naukkarinen, E. Laurila and P. Rabe: Rapid high resolution X-ray topography with synchrotron radiation, *Acta Polytechnica Scandinavica, Ph. Incl. Nucleonics* **100** (1973) 1–8.

[18] A. N. Danilewsky, R. Simon, A. Fauler, M. Fiederle and K. W. Benz: White beam X-ray topography at the synchrotron light source ANKA, Research Centre Karlsruhe, *Nucl. Instr. and Meth. B* **199** (2003) 71–74.

[19] R. Simon and A. N. Danilewsky: The experimental station for white beam X-ray topography at the synchrotron light source ANKA, Karlsruhe, *Nucl. Instr. and Meth. B* **199** (2003) 550–553.

[20] D. M. Mills, J. R. Helliwell, Å. Kvick, T. Ohta, I. A. Robinson and A. Authier: Report of the Working Group on Synchrotron Radiation Nomenclature – brightness, spectral brightness or brilliance?, *J. Synchrotron Radiation* **12** (2005) 385–385.

[21] H. O. Moser: A Guided Survey of Synchrotron Radiation Sources, in A. Chao, H. Moser and Z. Zhao (eds.), Accelerator Physics, Technology and Applications, World Scientific Publishing Co. Pte. Ltd. (2004) pp. 35–42.

[22] L. C. Teng: Synchrotron Radiation, in A. Chao, H. Moser and Z. Zhao (eds.), Accelerator Physics, Technology and Applications, World Scientific Publishing Co. Pte. Ltd. (2004) pp. 176–204.

[23] A. Koch, J. P. Moy and J. Morse: Detectors for synchrotron X-ray topography, *J. Phys. D: Appl. Phys.* **26** (1993) A19–A21.

[24] C. M. Castelli, N. M. Allinson, S. J. Barnett, G. F. Clark, K. Moon, C. R. Whitehouse and A. Wells: CCDs for X-ray topography at synchrotrons, *Nuclear Instr. Methods in Phys. Res. A* **391** (1997) 481–484.

[25] A. N. Danilewsky, A. Rack, J. Wittge, T. Weitkamp, R. Simon, H. Riesemeier and T. Baumbach: White beam synchrotron topography using a high resolution digital X-ray imaging detector, *Nucl. Instr. and Meth. B* **266** (2008) 2035–2040.

[26] T. Tuomi, K. Naukkarinen and P. Rabe: Use of synchrotron radiation in X-ray diffraction topography, *phys. stat. sol. (a)* **25** (1974) 93–106.

[27] T. Tuomi: Synchrotron X-ray topography of electronic materials, *J. Synchrotron Radiation* **9** (2002) 174–178.

[28] M. Moore: Synhrotron X-ray Topography, *Radiat. Phys. Chem.* **45** (1995) 427–444.

[29] T. Tuomi, M. Juvonen, R. Rantamäki, K. Hjelt, M. Bavdaz, S. Nenonen, M.-A. Gagliardi, P. J. McNally, A. N. Danilewsky, E. Prieur, M. Taskinen and M. Tuominen: Synchrotron x-Ray Topographic Study Of Dislocations In Gaas Detector Crystals Grown By Vertical Gradient Freeze Technique, *Mat. Res. Soc. Symp. Proc.* **487** (1998) 459–464.

[30] T. Tuomi, L. Knuuttila, J. Riikonen, P. J. McNally, W.-M. Chen, J. Kanatharana, M. Neubert and P. Rudolph: Synchrotron X-ray topography of undoped VCz GaAs crystals, *J. Cryst. Growth* **237–239** (2002) 350–355.

[31] J. Riikonen, T. Tuomi, A. Lankinen, J. Sormunen, A. Säynätjoki, L. Knuuttila, H. Lipsanen, P. J. McNally, L. O'Reilly, A. Danilewsky, H. Sipilä, S. Vaijärvi, D. Lumb and A. Owens: Synchrotron X-ray topography study of defects in indium antimonide P-I-N structures grown by metal organic vapour phase epitaxy, *J. Mat. Sci.: Mat. Elec.* **16** (2005) 449–453.

[32] P. J. McNally, J. Kanatharana, B. H. W. Toh, D. W. McNeill, T. Tuomi, A. N. Danilewsky, L. Knuuttila, J. Riikonen and J. Toivonen: Comparison of induced stresses due to electroless versus sputtered copper interconnect technology, *Semicond. Sci. Technol.* **19** (2004) 1280–1284.

[33] D. Noonan, P. J. McNally, W.-M. Chen, A. Lankinen, L. Knuuttila, T. O. Tuomi, A. N. Danilewsky and R. Simon: The evaluation of mechanical stresses developed in underlying silicon substrates due to electroless nickel under bump metallization using synchrotron X-ray topography, *Microelectronics J.* **37** (2006) 1372–1378.

[34] L. Xu, D. Lowney, P. J. McNally, A. Borowiec, A. Lankinen, T. O. Tuomi and A. N. Danilewsky: Femtosecond versus nanosecond laser micromachining of InP: a nondestructive three-dimensional analysis of strain, *Semicond. Sci. Technol.* **22** (2007) 970–979.

[35] H. Dosch: Evanescent absorption in kinematic surface Bragg diffraction, *Phys. Rev. B* **35** (1987) 2137–2143.

[36] H. DOSCH and H. REICHERT: Ordering, Disordering and Segregation at Binary Interfaces: Model System $Cu_3Au(001)$, *Acta mater.* **48** (2000) 4387–4393.

[37] W. K. BURTON, N. CABRERA and F. C. FRANK: Role of Dislocations in Crystal Growth, *Nature* **163** (1949) 398–399.

[38] T. A. READ: The Internal Friction of Single Metal Crystals, *Phys. Rev.* **58** (1940) 371–380.

[39] F. C. FRANK: Crystal Growth and Dislocations, *Adv. Phys.* **1** (1952) 91–109.

[40] F. C. FRANK: The Influence of Dislocations on Crystal Growth, *Disc. Faraday Soc.* **5** (1949) 48–54.

[41] F. C. FRANK and W. T. READ: Multiplication Processes for Slow Moving Dislocations, *Phys. Rev.* **79** (1950) 722–723.

[42] G. SCHOECK: Frank Read sources in semiconductors, *Acta Mat.* **55** (2007) 2043–2047.

[43] M. PEACH and J. S. KOEHLER: The Forces Exerted on Dislocations and the Stress Fields Produced by Them, *Phys. Rev.* **80** (1950) 436–439.

[44] D. CHERNS, W. T. YOUNG, J. W. STEEDS, F. A. PONCE and S. NAKAMURA: Observation of coreless dislocations in α-GaN, *J. Cryst. Growth* **178** (1997) 201–206.

[45] J. HEINDL, W. DORSCH and H. P. STRUNK: Dislocation Content of Micropipes in SiC, *Phys. Rev. Lett.* **80** (1998) 740–741.

[46] Y. ATICI: Defects generated by misfit strain in SiGe/Si(001), *Phys. Rev. B* **51** (1995) 13249–13255.

[47] B. RAGHOTHAMACHAR, G. DHANARAJ, J. BAI and M. DUDLEY: Defect Analysis in Crystals Using X-ray Topography, *Microscopy Research and Tehnique* **69** (2006) 343–358.

[48] B. K. TANNER: X-Ray Diffraction Topography, Pergamon Press (1976).

[49] A. R. LANG: Defect Visualisation: Individual Defects, in B. K. TANNER and D. K. BOWEN (eds.), Characterization of Crystal Growth Defects by X-Ray Methods, chap. 7, Plenum Press (1980) pp. 161–185.

[50] J. GEMPERLOVÁ, M. POLCAROVÁ and J. BRÁDLER: X-ray topographic contrast on dislocations with $g \cdot b = 0$, *J. Phys. D: Appl. Phys.* **26** (1993) A131–A136.

[51] M. Hart: Elemental Dynamical Theory, in B. K. Tanner and D. K. Bowen (eds.), Characterization of Crystal Growth Defects by X-Ray Methods, chap. 9, Plenum Press (1980) pp. 216–263.

[52] A. R. Lang: The early days of high-rsolution X-ray topography, *J. Phys. D: Appl. Phys.* **26** (1993) A1–A8.

[53] C. A. M. Carvalho and Y. Epelboin: Simulation of X-ray Topographs: a New Method to Calculate the Diffracted Field, *Acta Cryst. A* **49** (1993) 460–467.

[54] C. A. M. Carvalho and Y. Epelboin: Simulation of X-ray Traverse Topographs and Synchrotron Laue Topographs: Application of the Reciprocity Theorem, *Acta Cryst. A* **49** (1993) 467–473.

[55] H. Nagai: Structure of vapor-deposited $Ga_xIn_{1x}As$ crystals, *J. Appl. Phys.* **45** (1974) 3789–3794.

[56] W. M. Chen, P. J. McNally, K. Jacobs, T. Tuomi, A. N. Danilewsky, Z. R. Zytkiewicz, D. Lowney, J. Kanatharana, L. Knuuttila and J. Riikonen: Determination of crystal misorientation in epitaxial lateral overgrowth of GaN, *J. Cryst. Growth* **243** (2002) 94–102.

[57] T. Tuomi and K. Naukkarinen: Multiple diffraction lines in the synchrotron X-ray topographs of elastically bent silicon single crystals, *Phys. Rev. B* **24** (1981) 6125–6128.

[58] T. Tuomi, V. Kelhä, K. Naukkarinen and M. Blomberg: Multistereo Synchrotron X-ray Topography, *Z. Naturforsch.* **37a** (1982) 607–610.

[59] W. Shockley and W. T. Read: Quantitative Predictions from Dislocation Models of Crystal Grain Boundaries, *Phys. Rev.* **75** (1949) 692–692.

[60] W. T. Read and W. Shockley: Dislocation Models of Crystal Grain Boundaries, *Phys. Rev.* **78** (1950) 275–289.

[61] D. J. Eaglesham, D. M. Maher, E. P. Kvam, J. C. Bean and C. J. Humphreys: New Source of Dislocations in $Ge_xSi_{1-x}/Si(100)$ Strained Epitaxial Layers, *Phys. Rev. Lett.* **62** (1989) 187–190.

[62] Y. H. Lo: New approach to grow pseudomorphic structures over the critical thickness, *Appl. Phys. Lett.* **59** (1991) 2311–2313.

[63] J. Narayan and S. Oktyabrsky: Formation of misfit dislocations in thin film heterostructures, *J. Appl. Phys.* **92** (2002) 7122–7127.

[64] L. Vegard: Die Konstitution der Mischkristalle und die Raumfüllung der Atome, *Zeitschrift für Physik* **5** (1921) 17–26.

[65] J. W. Matthews, S. Mader and T. B. Light: Accommodation of Misfit Across the Interface Between Crystals of Semiconducting Elements or Compounds, *J. Appl. Phys.* **41** (1970) 3800–3804.

[66] J. W. Matthews and A. E. Blakeslee: Defects in epitaxial multilayers - I. Misfit dislocations, *J. Cryst. Growth* **27** (1974) 118–125.

[67] J. W. Matthews and A. E. Blakeslee: Defects in epitaxial multilayers - II. Dislocation pile-ups, threading dislocations, slip lines and cracks, *J. Cryst. Growth* **29** (1975) 273–280.

[68] J. W. Matthews and A. E. Blakeslee: Defects in epitaxial multilayers - III. Preparation of almost perfect multilayers, *J. Cryst. Growth* **32** (1976) 265–273.

[69] J. P. Hirth: Some Current Topics in Dislocation Theory, *Acta mater.* **48** (2000) 126–133.

[70] J. W. Matthews: Accommodation of Misfit Across the Interface Between Crystals of Semiconducting Elements or Compounds, *J. Vac. Sci. Technol.* **12** (1975) 126–133.

[71] A. Fischer, H. Kühne and H. Richter: New Approach in Equilibrium Theory for Strained Layer Relaxation, *Phys. Rev. Lett.* **73** (1994) 2712–2715.

[72] D. C. Houghton, D. D. Perovic and J.-M. B. G. C. Weatherly: Misfit strain relaxation in Ge_xSi_{1-x}/Si heterostructures: The structural stability of buried strained layers and strained-layer superlattices, *J. Appl. Phys.* **67** (1990) 1850–1862.

[73] D. C. Houghton: Strain relaxation kinetics in $Si_{1-x}Ge_x$/Si heterostructures, *J. Appl. Phys.* **70** (1991) 2136–2151.

[74] A. Rockett and C. J. Kiely: Energetics of misfit- and threading-dislocation arrays in heteroepitaxial films, *Phys. Rev. B* **44** (1991) 1154–1162.

[75] D. J. Paul: Si/SiGe heterostructures: from material and physics to devices and circuits, *Semicond. Sci. Technol.* **19** (2004) R75–R108.

[76] G. A. Slack and S. F. Bartram: Thermal expansion of some diamondlike crystals, *J. Appl. Phys.* **46** (1975) 89.

[77] I. Kudman and R. J. Paff: Thermal expansion of InGaP alloys, *J. Appl. Phys.* **43** (1972) 3760.

[78] J. F. C. Baker and M. Hart: An absolute measurement of the lattice parameter of germanium using multiple-beam X-ray diffractometry, *Acta Crystallogr.* **31a** (1975) 364–367.

[79] S. Kishino: Improved Techniques of Lattice Parameter Measurements Using Two X-Ray Beams, *Adv. X-Ray Anal.* **16** (1973) 367.

[80] G. Giesecke and H. Pfister: Präzisionsbestimmung der Gitterkonstanten von AIIIBv-Verbindungen, *Acta Crystallogr.* **11** (1958) 369–371.

[81] M. J. Matragrano, V. Krishnamoorthy, D. G. Ast and J. R. Shealy: Characterization and elimination of surface defects in GaInP, *J. Cryst. Growth* **142** (1994) 275–283.

[82] M. J. Matragrano, D. G. Ast, J. R. Shealy and V. Krishnamoorthy: Anisotropic strain relaxation of GaInP epitaxial layers in compression and tension, *J. Appl. Phys.* **79** (1996) 8371–8378.

[83] M. K. Lee, R. H. Horng and L. C. Haung: MOCVD Growth of GaInP Ordered Alloy by Phosphine Modulation, in Metalorganic Vapor Phase Epitaxy, Sixth International Conference, pp. 258–259.

[84] S. Hasenöhrl, R. Kudela, J. Novak, T. O. Tuomi and L. Knuuttila: Anisotropic surface structure in ordered strained InGaP, *Materials Science and Engineering B* **88** (2002) 134–138.

[85] D. C. Chapman, G. B. Stringfellow, A. Bell, F. A. Ponce, J. W. Lee, T. Y. Seong, S. Shibakawa and A. Sasaki: Nitrogen surfactant effects in GaInP, *J. Appl. Phys.* **96** (2004) 7229–7234.

[86] J. Novák, S. Hasenöhrl, R. Kúdela and M. Kučera: Growth and characterisation of InGaP layers with composition close to crossover from direct to indirect band gap, *J. Cryst. Growth* **275** (2005) e1281–e1286.

[87] B. Galiana, E. Barrigón, I. Rey-Stolle, V. Corregidor, P. Espinet, C. Algora and E. Alves: Compositional analysis and evolution of defects formed on GaInP epilayers grown on Germanium, *Superlattices and Microstructures* **45** (2009) 277–284.

[88] I. Beinik, B. Galiana, M. Kratzer, C. Teichert, I. Rey-Stolle, C. Algora and P. Tejedor: Nanoscale electrical characterization of arrowhead defects in GaInP thin films grown on Ge, *J. Vac. Sci. Technol. B* **28** (2010) C5G5–C5G10.

Aalto-DD 173/2012

BUSINESS +
ECONOMY

ART +
DESIGN +
ARCHITECTURE

SCIENCE +
TECHNOLOGY

CROSSOVER

DOCTORAL
DISSERTATIONS